Multiscale Foam Dynamics:
Stability Mechanisms in Salty Solutions

by

©Tatsuo Izawa

A Dissertation submitted to the School of Graduate Studies in partial fulfillment of
the requirements for the degree of

Master of Science (Physics)

Department of Physics and Physical Oceanography

Memorial University of Newfoundland

August 2017

St. John's   Newfoundland

Abstract

An oilfield is a region that is generally part of a sedimentary geological formation, made up of porous and permeable rocks, and bounded by impermeable barriers. A fluid is injected to displace the trapped oil. Most fluids are less viscous than the oil, where they are prone to pierce through the porous rock. When pressurized in an attempt to displace the oil, they pierce through the oil in an instability known as viscous fingering. Therefore, identifying appropriate candidate fluids is an essential step in improving oil recovery rate.

In this thesis work, an aqueous foam is chosen as a candidate fluid for investigation. A collection of free drainage studies has been conducted to gain deeper understanding of foams' ageing processes at different temporal and spatial scales. A commercially available nonionic surfactant, Triton X-100, has been used to produce foams. First, container effects are investigated to study how bulk foam dynamics change in differently shaped and sized containers. Second, an optical imaging system is developed to study the multi-scale dynamics of aqueous foam. Finally, using the newly developed optical imaging system, experiments at different salinities are conducted to study the salinity dependence on foam stability at different temporal and spatial scales. This information will likely impact the design of foam stability testing methods and contribute to the understanding of high salinity bubble interactions.

Acknowledgements

I would like to thank a number of people who were knowingly or unknowingly supported me throughout my time at Memorial University.

My supervisors, Dr. Lesley James and Dr. Anand Yethiraj for their patience, continuous support and encouragement for the last two years, and also for providing me with an opportunity to engage in science and for introducing me to the field of foams.

Dr. Stephanie Curnoe, for being on my thesis committee and for being an advisor who is willing to listen to our voices in the department. I am also grateful to faculty members, administrative staffs, instructional assistants in the department for having me around, and also for providing teaching opportunities to serve as a TA for the students in their lab courses. The machine shop and glass shop technicians are greatly acknowledged for their assistance with my research project.

Dr. Kristin Poduska, Dr. Ivan Saika-Voivod and their group members, for the interesting group discussions at our joint group meetings and for providing useful feedback on my talks. My Soft Matter colleagues, for their support and for great times in and outside of the lab. My office-mates, colleagues in the department and friends in St.John's. My EOR colleagues, especially Edison, for offering me to let me use the camera when I needed it (even on weekends) and for providing all the safety trainings in the lab.

Table of Contents

List of Abbreviations and Symbols

ϕ liquid volume fraction

ϕ_c critical liquid volume fraction

$\langle \rangle$ expectation value or mean

A bubble area (mm^2)

$1D$ one-dimensional

$2D$ two-dimensional

$3D$ three-dimensional

CMC critical micelle concentration

$Mass_{surf}$ mass of the surfactant solvent (g)

MW molecular weight (g/mol)

V volume of a solution (L)

C molar concentration (mol/L or M)

n number of ethylene oxide units

$wt\%$ weight of solute per weight of solution (%)

ppm parts per million

S initial liquid height (mm or otherwise indicated)

$L(t)$ liquid height (mm or otherwise indicated) as a function of time (s)

$T(t)$ total height (mm or otherwise indicated) as a function of time (s)

IFT interfacial tension (mN/m)

K mean bubble area growth rate (mm^2/s)

Chapter 1

Background and Theory

In this chapter, aqueous foams and characterization methods are introduced, followed by a motivation for the salinity dependence study, which is the focus of this thesis work.

1.1   Aqueous Foams

An aqueous foam is a dispersion of tightly packed gas bubbles in a continuous liquid-medium. These gas bubbles are separated by a thin film of liquid, which requires the use of stabilizing agents, such as surfactant molecules, to stabilize the foam. Surfactant molecules are amphiphilic molecules that have a polar head and a long carbon chain for a tail. The head is water-loving hydrophilic that faces towards the liquid film, while the tail is water-hating hydrophobic that faces away from the liquid film. They are arranged in a way that minimizes the total free energy of the system.

The individual constituents of an aqueous foam, gas and liquid, are fluids that are formless. A mixture of these fluids as a binary state of matter exhibits an emergent property that gives some solid-like characteristics in its entity, which is viscoelastic in nature. Aqueous foams behave like a fluid that flows, but also have a quality of a solid

that have a structure. A range of these complex properties of foams attract scientists to study their structure and dynamics within the context of disordered materials, complexity and soft matter [1]. Aqueous foams can be studied at different length-scales, as shown in Figure 1.1. Going from left to right in Figure 1.1, the largest scale of the aqueous foam (left) is typically in the range of centimeter to meter. The size of the bubbles ranges from a few micrometers to a centimeter. Thin liquid films range from a couple hundred nanometer to a millimeter, and the size of the molecules is around a nanometer.
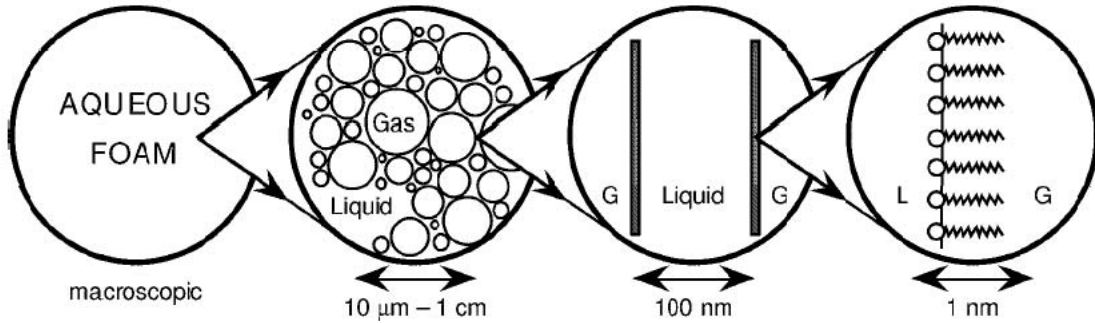

Figure 1.1: Lengthscales in an aqueous foam (left to right) from the whole foam to the bubble scale to the film scale to the molecular scale. An image adapted from [2].

1.2 Foam Stability Mechanisms

Foam stability comprises of three mechanisms that determine their aging processes: drainage, coarsening, and coalescence (also known as film rupture). A three-dimensional ($3D$) foam consists of cells whose faces are two-dimensional ($2D$) films. These faces meet at one-dimensional ($1D$) channels, which are known as Plateau borders. In the presence of gravity, drainage occurs when the excess liquid drains out through the Plateau border channels until an equilibrium state is reached in a foam. Under this free drainage condition, drainage, coarsening and coalescence happen concurrently at different timescales, and these phenomena are hard to decouple. Studying the mecha-

nisms individually still remains a challenge with the ever-present gravity drainage on earth. There is an ongoing research effort to conduct foam research in outer space in order to decouple these mechanisms in a gravity-free environment [3].
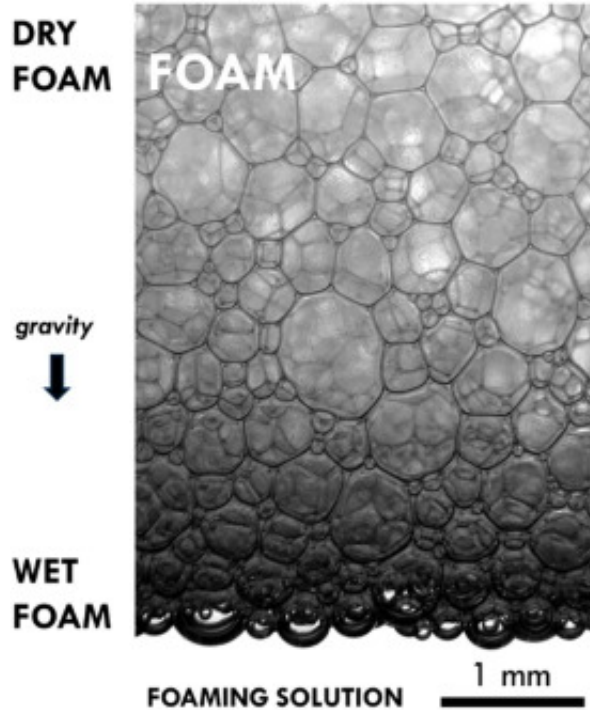

Figure 1.2: An aqueous foam under gravity, where polydispersity is more pronounced at the top. Image modified from [4].

Figure 1.2 illustrates the whole foam that qualitatively distinguishes different regions in a foam: the highly faceted dry foam region at the top, the wet foam region at the bottom, and the intermediate region in-between. Depending on the region of the foam, dry and wet foam regions can be classified by liquid volume fraction, ϕ, as depicted in Figure 1.3. When ϕ is less than 1%, the foam may be called dry [1, 3]. When ϕ is greater than 10%, the foam may be called wet [3]. The geometrical aspects of the bubbles pose an important information as a consequence to the liquid volume fraction. In the very dry limit, $\phi \to 0$ and bubbles are polyhedra with thin curved faces that meet at Plateau borders. In the very wet limit, $\phi \to 1$ and bubbles are

3

round and far from each other [5]. A critical liquid volume fraction, ϕ_c, exists at around 30% above which spherical shaped bubbles can move independently [5], which we call bubbly liquid instead of foam. This critical ϕ_c value depends on whether the foam is disordered ∼35% or ordered ∼25% [3]. At ϕ_c, foam behavior changes from solid-like to liquid-like, where the lower liquid fraction ("air" side) of the foam is the solid-like extreme. This transformation is known as the jamming transition, as indicated in Figure 1.3.
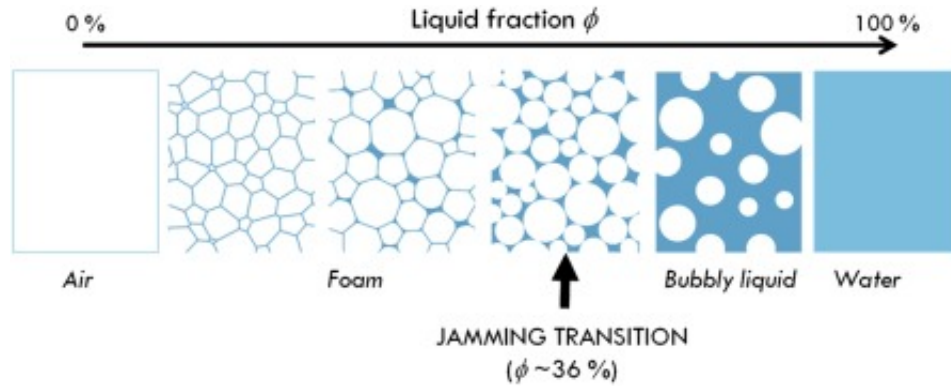
Figure 1.3: Bubble images of a foam for different liquid fractions. An image adapted from [3].

To address foam stability, one can look at different scales of a foam. At the macroscopic scale, we can look at how long the foam lasts before it collapses back to the foaming solution. In a foam system where a pressure difference exists between adjacent bubbles, the gas diffuses through the interface until the bubble at higher pressure completely disappears while the bubble at lower pressure increases in size [6]. On average, where there are a large number of bubbles packed together, the average bubble diameter grows with time, as illustrated in Figure 1.4.
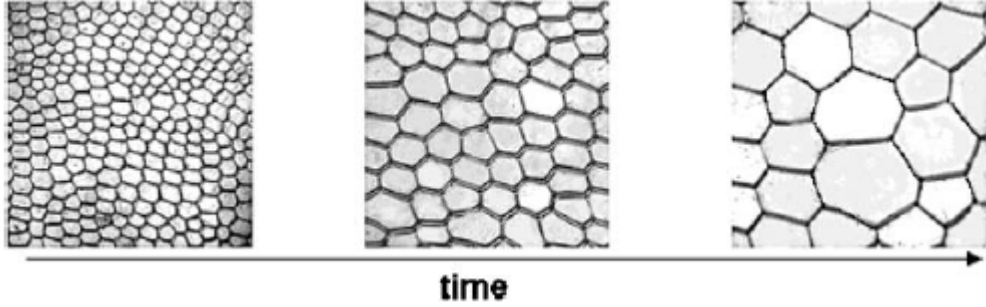
Figure 1.4: A sequence of bubble coarsening events [7].

This coarsening behavior varies depending on the liquid volume fraction. In the dry limit, the coarsening growth rate follows the law of von Neumann and Mullins [8], which is exact in two dimensions, and describes the time dependence of the average bubble diameter:

$$\langle d(t) \rangle \sim t^{1/2}. \tag{1.1}$$

The von Neumann-Mullins scaling, Equation 1.1, has been generalized to coarsening in a 3D foam [8], and many experiments support this scaling law both in 2D and 3D [1, 9]. In the wet limit, the coarsening of bubbles in bubbly liquid undergoes Ostward-Lifschitz-Slyozov-Wagner ripening in 3D and Ostwald-Marqusee and Ostwald-YEGG in 2D [5], where

$$\langle d(t) \rangle \sim t^{1/3} \tag{1.2}$$

Film breaking events are well observed phenomena in foams, which we call coalescence, where the foams undergo collapsing due to film rupture of the interface, as shown in Figure 1.5. This has most often been observed at the top free surfaces of the 3D foam, where the films are the thinnest.

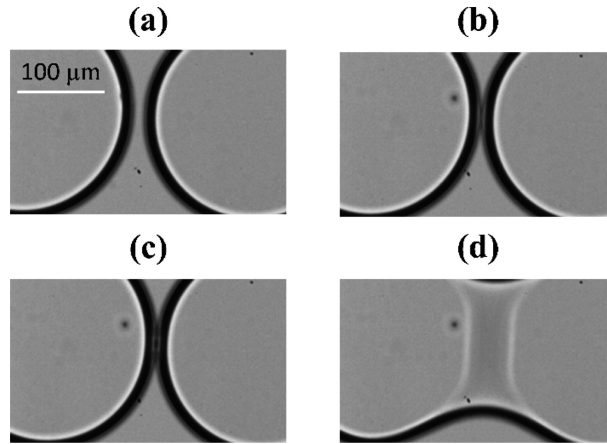Figure 1.5: An image sequences of bubble coalescence in different stages [10]. Two bubbles approach (a) and then contact (b). Liquid film drains (c) between the bubbles as the bubble coalescence starts to occur (d).

1.3   Previous Studies on Foam Stability

In search of a reliable foam stability characterization method, there is always a competition between its practicality and its optimal condition for theoretical modelling. For practicality, we adapted the use of the simple shaking method with a foaming solution in a closed bottle, as outlined in the technical report (ASTM D3601) [11] with a specific shaking frequency, amplitude, and duration, similar to the Bartsch shaking test, as described in [12]. The quantity one would obtain is a bulk scale measurement, either the height of the foam or the volume of the foam in a column, to study its dynamics. Moayedi [13] and Andrianov and others [14] adapted the manual recording for their bulk scale foam dynamics studies, where they manually measured the foam height using a ruler outside of a bottle and a graduated glass cylinder, respectively. Binks and Horozov [15] extended this manual recording method to an imaging technique for their bulk foam stability study. There are others who focused their research on applying bubble scale imaging techniques to capture dynamics of 2D model foams in a confined geometry. All of these studies aimed to understand the foam stability

6

either at the macroscopic or the microscopic level, but not both at the same time.

To address bulk and bubble scale dynamics of different foams, Osei-Bonsu and others [16] obtained the bulk scale and bubble scale features of the foams of their interest separately for their foam stability study. For bulk scale, they used a 1 m column, while for bubble scale, they used a Hele-Shaw cell, a quasi-2D bubble imaging apparatus consisting of two plexiglass plates with a backlight and a small gap for the sample foam to be confined, which restricts its dynamics.

Ideally, one would like to conduct such a study using a simultaneous imaging method. This has, however, never been performed due to the difficulty in applying imaging on $3D$ foam dynamics, in general, as briefly discussed in [17]. To our knowledge, there is no study conducted using the simultaneous bulk and bubble-scale method in the field of foam stability methodologies. As well, Papara and others [18] looked at the container effects on free drainage of foams using different sized round containers. To our knowledge, there are also no comparative studies on free foam drainage for round and rectangular bottles, so the effects of different containers on aqueous foam have been less known. In this work, we first study the effect of bottle size and shape on bulk foam dynamics. We then apply a simultaneous imaging technique to conduct experiments on the free drainage of foam to study the aging processes at different temporal and spatial scales.

1.4   Stability in Salt Foams

For a system of colloidal particles, emulsion droplets or bubbles, it is well known that adding salts influences the electrostatic interactions between the particulates [19]. Unlike surfactants, the addition of salts is generally understood to promote bubble coalescence by classical theories, such as the Debye-Hückel and the Derjaguin-Landau-

Verwey-Overbeek theory [19]. These theories, however, only work well with low salt concentrations and do not incorporate ion-specificity in their theories [19]. Hofmeister's work in the 19th century came into the picture on the particle stability at high salt concentrations, where ion-specific effects dominate over the electrostatic interactions [20].

Craig and others [21] were the first to empirically show that bubble coalescence can be inhibited by certain types of salts, while some other salts do not show any effect on bubble coalescence. They assigned a property (α or β) to each anion or cation of their choice of ions, categorized their choice of salts into whether inhibition or no inhibition was observed, and proposed combining rules that provided insights into the ion-specific effects on bubble coalescence. A follow-up study by Henry and others [20] extended the list of the combining rules with additional electrolytes, as shown in Figure 1.6. While many possible mechanisms, such as electrical double layer repulsions [22], hydration repulsions [23], the Gibbs-Marangoni effect [24, 25], gas solubility and hydrophobic attractions [26] have been proposed to explain the inhibition mechanism of the ion-specific effect on bubble coalescence, there is no consensus on one mechanism, and the theoretical understanding of ion-specific effects on bubbles remains lacking [20, 27].

Ions		Li^+	Na^+	K^+	Cs^+	Mg^{2+}	Ca^{2+}	NH_4^+	H^+	$(CH_3)NH_3^+$	$(CH_3)_2NH_2^+$	$(CH_3)_3NH^+$	$(CH_3)_4N^+$
Assignment		α	α	α	α	α	α	α	β	β	β	β	β
OH^-	α		✓	✓					✗				
Cl^-	α	✓	✓	✓		✓	✓		✗	✗	✗	✗	✗
Br^-	α		✓	✓	✓				✗				✗
NO_3^-	α	✓	✓	✓			✓		✗				
SO_4^{2-}	α	✓	✓	✓		✓			✗				
$(COO_2)^{2-}$	α			✓					✗				
IO_3^-	α		✓										
ClO_3^-	β		✗										
ClO_4^-	β		✗			✗		✗	✓				
CH_3COO^-	β		✗	✗	✗	✗		✗	✓				✓
SCN^-	β		✗										

✓=inhibit coalescence ✗=no inhibition
$\alpha\alpha$, $\beta\beta$ = ✓
$\alpha\beta$ $\beta\alpha$ = ✗

Figure 1.6: Combining rules for bubble coalescence. Adapted from [20]

Craig and others [21] also performed experiments by increasing salt concentrations, where they observed a sharp transition from high percentage coalescence (between 90 and 100%) down to low percentage coalescence (0% and below) for salts that have shown to have an effect on bubble coalescence. The concentration at which this sharp decrease occurs is called the transition concentration. Based on their experimental evidence, they have shown that the salt contribution to the bubble coalescence is concentration-dependent, where a transition exists between no inhibition and a constant inhibition [20]. For inhibition observed salts, i.e. $\alpha\alpha$ or $\beta\beta$ salts as listed in Figure 1.6, 0.01 M of the salt solutions showed no effect on bubble coalescence relative to pure water. By increasing the salt concentration of the solution, they found that the maximum coalescence inhibition was shown to have reached by 0.2 M, above which adding more salts had no further effect to the bubble coalescence.

Understanding the effect of salts on bubble coalescence is of relevance to our foam stability study. Moreover, the concentration-dependent phenomenon observed requires further theoretical explanation, backed up by experimental evidence. Experimentally, we aim to contribute our work to the understanding of foam stability at high salt concentrations by addressing the following questions. Can we identify any physical mechanism behind the higher foam stability at high salt concentrations? Can bubble coalescence inhibition by high salt concentrations cause overall foam stability? What determines the stability of foam in the presence of salts in solutions? How do different salinity foams behave at different temporal and spatial scales? Are the physical parameters, such as bubble size and foam height, sufficient to define a foam? Can we predict its evolution without considering the chemical components? What microscopic parameters involved are important in understanding the foam's aging process. These are the physics questions one can ask for our deeper understanding of the foam stability mechanisms in the presence of salts.

1.5 Enhanced Oil Recovery for the Province of Newfoundland and Labrador

In the province of Newfoundland and Labrador, Canada, offshore platforms have been built to extract oil from the oilfields deep under the ocean. The oil and gas industry has opened up new opportunities for the people in the province, and has made significant contributions to the province's economic growth. Currently, the province has invested in four oilfield sites: Hibernia, Terra Nova, White Rose and Hebron [28]. One challenge is to recover as much oil as economically possible from the offshore fields. Seawater is typically injected for pressure maintenance (secondary recovery) and as part of enhanced oil recovery (EOR) methods such as water-alternating gas (WAG), polymer flooding, surfactant flooding and alkaline surfactant polymer (ASP) flooding. Reservoir brine has much higher salts concentrations than seawater because of the minerals dissolved from the rocks over geological time.

When a fluid is injected into the porous media of rocks in the reservoir well, one needs to consider fluid-fluid interactions, mainly between the injected fluid and the oil trapped inside of the rocks in the reservoir well. A most common issue here is a fingering effect due to an instability that occurs when a less viscous fluid, such as water or air, is injected to displace more viscous fluid, such as oil. This effect is known as the viscous fingering effect [29].

Due to the viscoelastic property of aqueous foams, they have been considered as a potential injection fluid to combat the viscous fingering effect with the oil [30, 31]. Therefore, a deeper understanding of foam stability in the presence of high salinity seawater and formation reservoir brine is important for enhanced oil recovery. Another important aspect, not considered in this work, is foam stability in the presence of hydrocarbons [16].

In this work, we aim to experimentally uncover mechanisms for bulk scale and bubble scale dynamics of 3D foams at a surface at different brine salinities, including the ocean brine and the reservoir brine concentrations. To stabilize the foam, we use a well characterized non-ionic surfactant, Triton X-100 [32].

Chapter 2

Experimental Methods

In this chapter, I first describe in detail how foaming solutions are prepared. I then describe how experimental conditions are optimized for the multiscale dynamics study at different salinities. Optical imaging techniques and other fluid characterization methods are also discussed. The goal of this section is not only to present how foams are prepared, but also to provide some suggestions to relevant industries on a foam characterization method.

2.1   Foam Preparation

To prepare aqueous foams and disperse air bubbles in a liquid, containers are necessary to support and to fully contain the foam fluid in a closed system. We prepare three containers of different shapes and sizes before foaming solutions are made. In this section, we first present the bottle washing procedure. We then present how foaming solutions are prepared. The Standard Test Method for Foam In Aqueous Media (Bottle Test) [11] is a technical document that we follow to produce foams from the foaming solutions.

2.1.1 Bottle Washing

Glass containers are cleaned very carefully to avoid any contamination on the glassware, such that they are physically and chemically sterile. This includes the use of clean equipment that will be directly or indirectly exposed to the foams. The bottle washing process is essential not only for cleaning purposes, but also to avoid any small impurities that may lead to the alternation of the meniscus due to the presence of grease or other contaminants.

Most glass containers used in this study are brand new, and they are slightly alkaline in reaction [33]. Therefore, all of the containers and glassware are soaked in approximately 1% hydrochloric solution for several hours before performing further treatment. The glassware is washed by running hot tap water several times, and scrubbing gently and thoroughly with a brush. An anionic surfactant based detergent is commonly used at this point; however one must be careful not to allow detergent to interact with the acid residues due to possible formations of greasy materials on the glassware. A powder-based concentrated anionic detergent, "ALCONOX", was used throughout the study. As a final step, the glassware is filled with deionized water and then sonicated in a ultrasonic bath for a few minutes. The containers are rinsed again with deionized water, and are again completely dried without using any air dryer, on a flat surface naturally over time.

2.1.2 Foaming Solution Preparation

Aqueous foams are prepared for five different salt concentrations with the same amount of nonionic surfactant in each solution to carry out the free foam drainage experiments. Triton X-100 surfactant, also known as octylphenol ethoxylate, is the

nonionic surfactant of interest throughout our studies. It has been widely used as a detergent for several applications, including industrial cleaners, and as oilfield, textile and metalworking fluids [34].

The chemical formula of Triton X-100 is $(C_8H_{17})C_6H_4(OCH_2CH_2)_nOH$, where $(OCH_2CH_2)_nOH$ is the ethylene oxide unit. The number n of ethylene oxide units in its chemical formulae ranges from 9 to 10 [32, 34–36]. This means that depending on the choice of n value, its molecular weight varies between 602.784 g/mol and 646.836 g/mol. The choice of the molecular weight has an impact on the overall mass of surfactant solvent needed to be added to make surfactant solutions. Thus, a calculation needs to be performed to compare among three commonly reported values using Equation 2.1.

$$Mass_{surf} = MW \times V \times C, \tag{2.1}$$

where $Mass_{surf}$ is the mass of the required surfactant solvent added to make a solution, MW is the molecular weight (g/mol) of the surfactant used, V is the final volume of the solution (L), and C is the molar concentration (mol/L) of the surfactant.

The first critical micelle concentration (CMC) of Triton X-100 surfactant is reported to be between 0.19 mM and 0.27 mM [37–41]. This discrepancy is likely from different characterization methods across laboratories, as listed in the references. Small variations in the composition and properties of Triton X-100 from different manufacturers are discussed in [42]. For the purpose of our study, we use a CMC value of 0.25 mM (or 0.00025 mol/L) and n of 9.5. The variation in molecular weight allows us to establish the uncertainty associated with the surfactant amount added to make a solution. Previous work done by Moayedi et al. [13] reported the use of the first CMC value of the Triton X-100 plus 0.3 weight percent to prepare foams using the Standard Test Method for Foam in Aqueous Media [11], also known as the Bottle Test. Until the year 2013, the petroleum industry had been utilizing the method as a

way to visualize and to study the lifetime of foams. As of the year 2013, this method had been withdrawn [11].

	molecular weight (g/mol)	surfactant concentration (mol/L)
$n = 9$	602.784	0.00496±0.00008
$n = 9.5$	624.810	0.00478±0.00008
$n = 10$	646.836	0.00462±0.00007

Table 2.1: Molecular weight and surfactant concentration comparisons among the choice of the number of ethylene oxide units. Note: These surfactant concentration sample values are obtained using the density value of Triton X-100 of 1.06±0.01 g/mL measured using a densitometer, and the total volume of the Triton X-100 surfactant of 2.82 ± 0.01 mL in 1 kg of solution without any salts. Sample: Triton X-100 $CMC + 0.3 \, wt\%$ solution

In our study, we obtain the density of the Triton X-100 solution at $CMC + 0.3 \, wt\%$ to be 0.9993±0.0005 g/mL. The purpose of this added surfactant is to test the foam stability much above its CMC value, as discussed in [13]. The surfactant concentration of $CMC + 0.3 \, wt\%$ will therefore be equivalent to 0.0047±0.0002 mol/L. Next, different salt concentrations of synthetic brine are prepared as shown in Table 2.3. According to the U.S. Geological Survey [43], the salt concentrations can be classified into 5 categories in parts per million (ppm). Fresh water is classified as brine concentration less than 1000 ppm. Slightly saline water ranges between 1000 ppm and 3000 ppm. Moderately saline water ranges between 3000 ppm and 10000 ppm. Highly saline water ranges between 10000 ppm and 35000 ppm. For our study, we tested with 0 ppm, 7000 ppm, 21000 ppm, 35000 ppm and 107132 ppm (standard reservoir brine concentration of EOR laboratory), as listed in Tables 2.2 and 2.3.

salt molarity (mol/L)	salt concentration (ppm)	weight$_{salt}$ per weight$_{total}$ (g/kg)
0	0	0
0.01124	7000	7
0.03399	21000	21
0.05716	35000	35
0.18366	107132	107.132

Table 2.2: Values of the different salinity samples in different units

composition	composition (%)	fresh water (gram)	moderate (gram)	high (gram)	ocean brine (gram)	Offshore NL brine (gram)
NaCl	84.4	0	5.906	17.719	29.532	90.397
$CaCl_2 \cdot 2\,H_2O$	12.3	0	0.863	2.588	4.313	13.202
$MgCl_2 \cdot 6\,H_2O$	2.6	0	0.180	0.541	0.902	2.760
KCl	0.4	0	0.028	0.084	0.140	0.429
$Na_2 \cdot (SO_4)$	0.3	0	0.023	0.068	0.113	0.345
total salinity (g/kg)	100	0	7.000	21.000	35.000	107.133

Table 2.3: Composition of an offshore Newfoundland reservoir brine (synthetic brine) at different salinities. All of the values are in grams per kilogram of solution.

2.2 Optimization of Experimental Conditions

The method we develop to optimize experimental conditions allows us to study how bulk foams behave in glass container bottles with different size and shape, and to identify an appropriate bottle to be used for further free drainage experiments. In this section, we first introduce two main experimental conditions that need to be considered to minimize characteristic bottle effects on foams and to develop a methodology for studying aging processes of foams.

2.2.1 Tests of Container Dependence

We study 3 types of glass container bottles in various shapes and sizes by studying the free drainage of foam using a simple optical imaging technique in a straight transmission geometry. In this optical geometry, the foams in the 3 glass bottles are illuminated using an LED monitor, simultaneously side by side, in a straight optical axis. The light passes through the bulk foam, which is then captured by a camcorder (JVC 100) at 1 frame per second.

The detail of the three different bottles is listed in Table 2.4. Width, length and diameter are measured from the exterior of the bottles using a 30-cm ruler. The bottle total height (TH) is the height of the bottles that include the well-sealed cap. The allowed bottle height (Ha) is the height of the bottles from the glass bottom of the bottles up to a level beyond which they start to have curvature towards the mouth of the bottles. The bottle base height (Hb) is the height of the glass bottom of the bottles. All height measurements are with reference to the table on which the bottles stand. The bottle mass (M_{bot}) is the mass of a bottle including the cap well sealed.

	Boston Round Bottle (16 oz)	French Square Bottle (16 oz)	French Square Bottle (32 oz)
width (W) / diameter (D)	7.0±0.1 cm	6.5±0.1 cm	8.0±0.1 cm
length (L) / diameter (D)	7.0±0.1 cm	6.5±0.1 cm	8.0±0.1 cm
total bottle height (TH)	17.5±0.1 cm	17.0±0.1 cm	20.6±0.1 cm
allowed bottle height (Ha)	12.5±0.1 cm	13.0±0.1 cm	15.5±0.1 cm
bottle base height (Hb)	0.8±0.2 cm	0.5±0.2 cm	0.7±0.3 cm
bottle mass (M_{bot})	301.6±0.1 g	306.2±0.1 g	456.0±0.1 g

Table 2.4: Specifications of the glass containers used.

In Figure 2.1, a schematic of a foaming solution containing bottle is shown before and after the bottle is shaken. The initial liquid height (S) is the height from the container bottom measured from the table up to the meniscus at the liquid-gas interface without a foam being created. After the foam has been created, we define the Liquid Height $(L(t))$ as the liquid level reduced due to foaming as a function of time. We also define the Total Height $(T(t))$ as the sum of the liquid and foam heights as a function of time. A foam has a wet region, where the liquid content is higher, and a dry region, where there is low liquid content in the foam. As outlined in the Bottle Test procedure [11], the bottle containing the foaming solution is shaken 40 times under 10 seconds for all experiments.
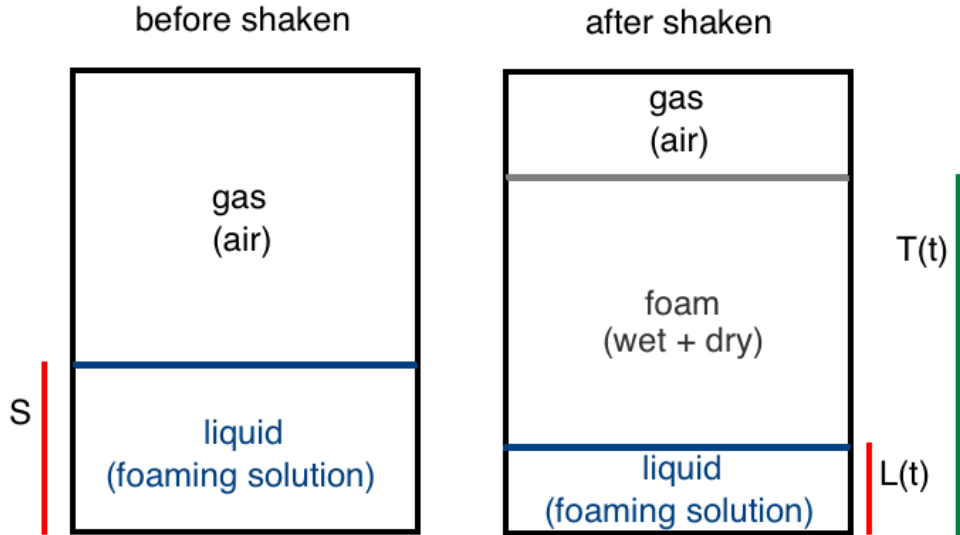

Figure 2.1: Schematics of foaming solution showing the working notation for various measured heights in the foam.

2.3 Dual Scale Foam Dynamics

In this section, we discuss a construction of the simultaneous imaging technique that probes macroscopic and microscopic features of a foam. We use this setup for our study of the foams. We also discuss different fluid characterization techniques.

2.3.1 Density, Surface Tension and Viscosity Measurements

A hand-held densitometer (DMA-35, Anton Paar) is used to measure the density of the foaming solutions. This densitometer operates based on the oscillating U-tube principle, where the device electronically excites a U-shaped borosilicate glass tube and induces a resonant frequency [44]. Since the liquid sample goes through the U-tube, we know the volume of the sample. To obtain the mass for density measurement, it utilizes the inverse proportionality between the resonant frequency and the square root of its mass. An interfacial tension meter (Vinci IFT 700) is used to measure the surface tension of the foaming solutions in air. The Vinci IFT 700 uses the pendant/rising drop methods that allow the measurement of the interfacial tension of two immiscible fluids. A rheometer (Anton Paar MCR 301) is used to measure the shear stress as a function of shear rate to obtain the viscosity of the foaming solutions.

2.3.2 The Optical Imaging System Construction

We develop an imaging system that probes bulk-scale and bubble-scale features of the foam dynamics using two cameras, as shown in Figure 2.3. For bulk-scale imaging, we use a set of crossed polarizers, i.e., at 90 degrees from each other, with collimated transmitted light using an illumination source (an LED monitor at a 70% Red, 70% Green, and 70% Blue light intensity setting). Crossed polarizers are used to reduce the background noise and to optimize the use of the foam's optically anisotropic feature. For bubble-scale imaging, we use the same illumination source as used for the bulk-scale imaging from a side that is slightly tilted to capture the surface features of the foam using a water-filled triangular prism that has a higher refractive index ($1.32 \leq n \leq 1.52$) than the air ($n \sim 1.00$). Since a foam consists of liquid and gas (air), when the foam is illuminated at a certain angle and above, the light that travels

towards a less refractive index (air) is reflected, as illustrated in Figure 2.2, by total internal reflection. In this technique, we only capture the bubble features of the foam, that is close to the interior surface of the bottle.

The triangular prism is hand-made using relatively large microscope glass plates and deionized water: three rectangular glass plates (approximately 5 cm x 13 cm) and two triangular glass plates (approximately 7 cm each side) for the bottom and the top enclosure. One of the rectangular glass plates is carefully glued first to one side of the glass bottle (16 Oz French square bottle) using an UV optical adhesive. The plate needs to be carefully attached to the bottle to avoid introducing air bubbles. Viscous fingering can be observed with the less viscous fluid, the air, and the more viscous fluid, the adhesive. The quality of the construction will have great impact on the bubble scale measurement. Then, the rest of the two rectangular glass plates and the bottom triangle plate are glued using the UV optical adhesive, stabilized for the triangular prism shape and exposed under an UV lamp for a couple of hours.

The novelty of this work is this: The slightly tilted illumination source allows the light to be guided to the interior surface of the foam containing glass bottle to the bubble-scale CCD camera via the triangular prism, while allowing the light to travel through the foam for bulk-scale imaging. This configuration of the illumination source with respect to both cameras allows the light to minimize light scattering from the foam to the illuminated surface from the back for the bubble-scale imaging.
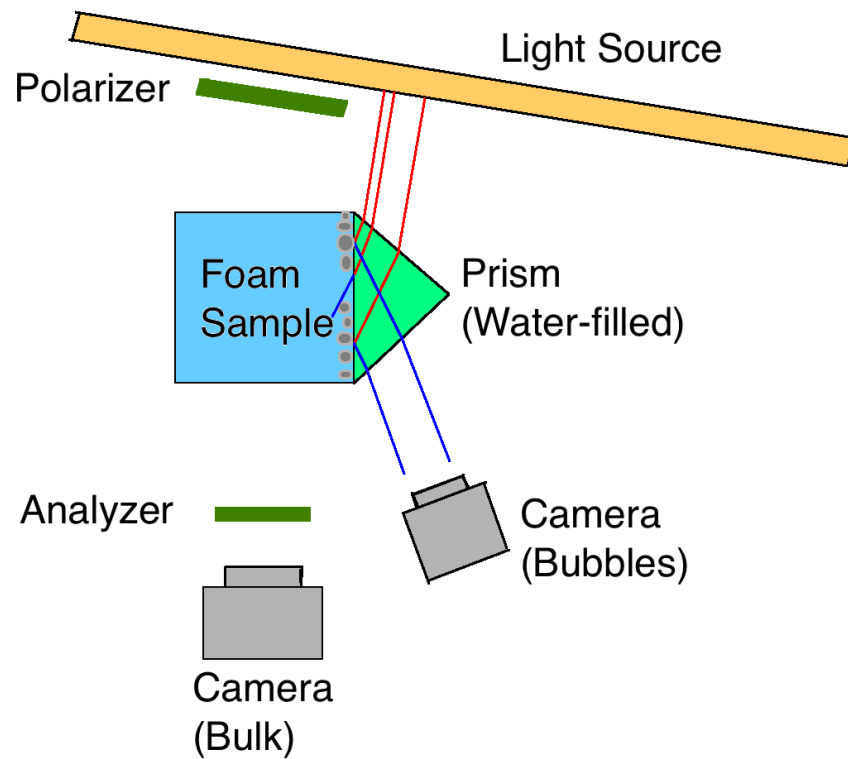
Figure 2.2: A schematic of a simultaneous imaging setup for bulk and bubble scale imaging. The distance between the light source to the foam sample is approximately 20 cm, and the distance between the foam sample to the bulk imaging camera is approximately 20 cm. The polarizer and analyzer are set up right in front of the light source and the camera, respectively. Note: Since the monitor is already polarized, the polarizer was drawn to show the crossed pair of polarizers for the bulk scale imaging.

Chapter 3

Results on Foam Stability and Bubble Size

In this section, I first address the question of how bulk scale foam evolves differently in three different sized and shaped containers. Once an appropriate container is chosen, I then further carry out experiments, using our dual-scale simultaneous imaging technique, to address how different saline levels of synthetic ocean brine affect their foam stability at the bulk (macroscopic) and bubble (microscopic) scales. Finally, I discuss how these macroscopic and microscopic features can be correlated.

3.1 Bulk Foam Dynamics

To determine an appropriate container for further foam stability studies, three different containers are tested: a Boston Round Bottle (16 oz), a small French Square Bottle (16 oz), and a large French Square Bottle (32 oz) to carry out the free foam drainage experiments. Since the three bottle containers cannot be shaken at the same time, the actual start times are different. The time durations are calculated by subtracting

the start times. As an example of the bulk foam analysis, bulk-scale snapshots of the height reduction in a foam at four times t = 0 s, 3000 s, 6000 s and 18000 s are shown on the top panel of Figure 3.1. The direction of gravity is pointed downwards in the top panel of the Figure 3.1 and it is pointed left in the bottom panel of Figure 3.1.
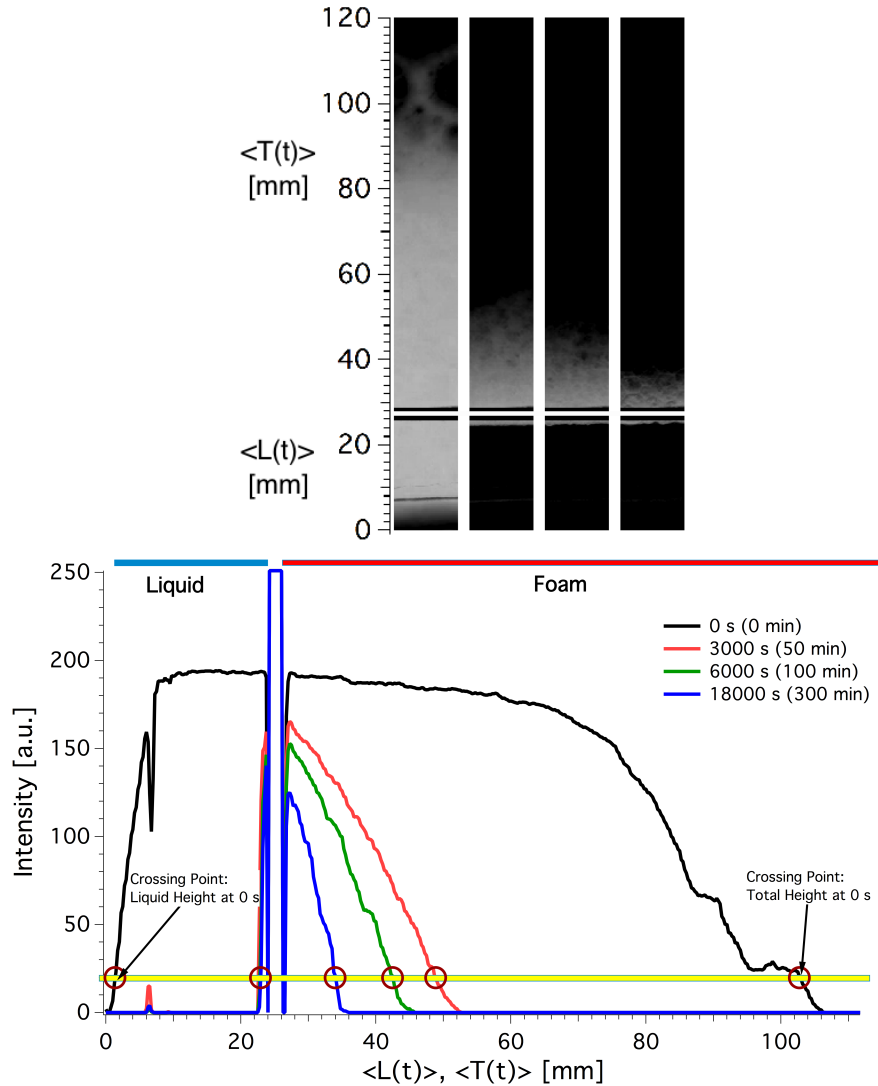

Figure 3.1: A sample bulk foam analysis of intensity profiles at different times t = 0 s, 3000 s, 6000 s and 18000 s. Top: White color indicates the foam in the bottle. Bottom: Intensity profiles of the foam plotted at different times. The yellow bar indicates a crossing level. The red circles indicate the crossing positions for height measurements. Sample: CMC + 0.3wt% (0.0047±0.0002 mol/L) of Triton X-100 surfactant in a 21 g/kg synthetic brine solution (total volume = 100 mL). The blue peak between 24 mm and 26 mm was drawn to divide regions of the liquid and the foam.

23

Each profile (bottom panel of Figure 3.1) represents the pixel-averaged foam intensity, denoted as $\langle \ \rangle$, over the entire inner width of the bottle container. Each image in the top panel yields a single curve in the plot on the bottom panel. The mean total height, denoted as $\langle T(t) \rangle$, is defined as the pixel-averaged foam level from the bottom of a container, and the mean liquid height, denoted as $\langle L(t) \rangle$, is defined as the pixel-averaged liquid level from the bottom of the same container. $\langle T(t) \rangle$ and $\langle L(t) \rangle$ at different times are obtained from the foam intensity profiles, as shown in the plot on the right panel of Figure 3.1. The obvious artifact on the plot between 24 cm and 26 cm is the region of liquid-air interface, the liquid meniscus, in the last frame. All frames are subtracted from the last frame and a vertical line has been added to distinguish between the liquid and the foam regions. This line is shown as a blue rectangular peak in the figure.

At t = 0 s, the intensity profile of scattered light shown by the black curve represents the foam when the container is stabilized in the imaging system after it is shaken. In order to define the total and liquid heights of a foam, a horizontal line of a common threshold level on the intensity profile is chosen across all intensity profiles. This level is slightly higher than the highest noise level from the intensity profiles at all times. With time, the intensity profiles become smaller and smaller, which shows that the foam ages on a macroscopic scale. This macroscopic ageing phenomenon is quantified in terms of the total and liquid heights with time, as shown in Figure 3.2.
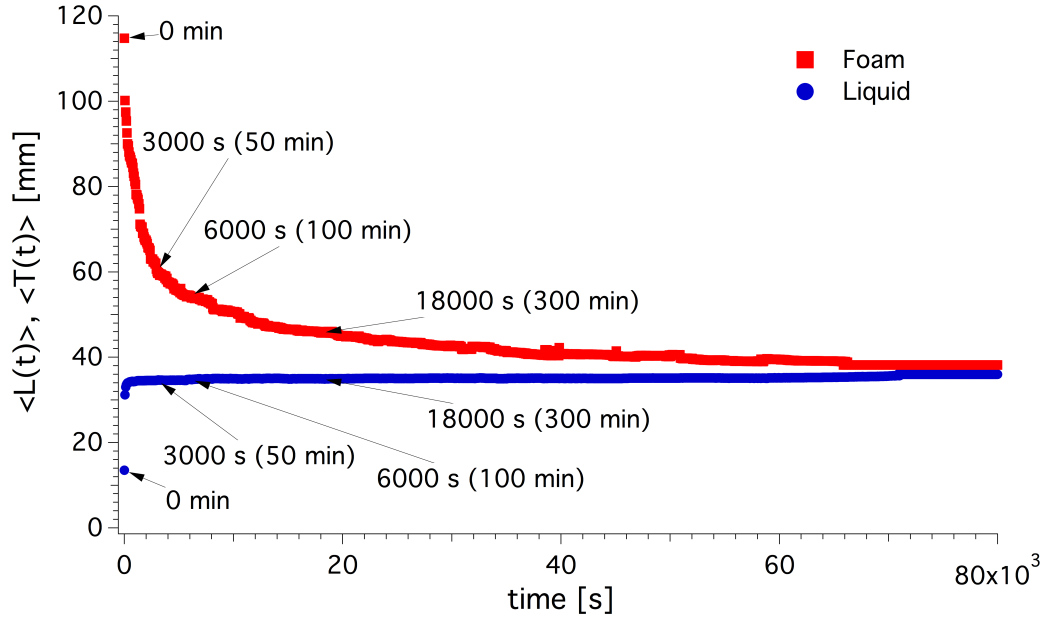
Figure 3.2: A plot of mean liquid, $\langle L(t) \rangle$, and mean total, $\langle T(t) \rangle$, heights over 80000 seconds following the crossing position analysis performed, as shown in Figure 3.1. Sample: CMC + 0.3wt% (0.0047±0.0002 mol/L) of Triton X-100 surfactant in a 21 g/kg synthetic brine solution (total volume = 100 mL).

The free foam drainage tests are performed to show the aging process for the three containers. The details of the containers are shown in Table 2.4 in the Experimental Method section. Shown in Figure 3.3 is a plot of the time dependence of the foam height that compares among 3 different glass containers, where the mean foam height is defined as the difference between the mean total height $\langle T(t) \rangle$ and the mean liquid height $\langle L(t) \rangle$, as follows.

$$\langle F(t) \rangle = \langle T(t) \rangle - \langle L(t) \rangle \tag{3.1}$$

At time t = 0 s, the mean foam height shows significant height differences among different containers. A small French Square Bottle results in significantly higher foam height than both the Boston Round Bottle and the 32 Oz French Square Bottle. Between the Boston Round Bottle and the 32 Oz French Square Bottle, the difference

25

in foam height is not significant. At around 1500 s (25 min), the foam height starts to converge for all glass containers; this is seen in Figure 3.3 (inset). On much longer times it is not possible to distinguish the foam height for different containers. The foam height for all containers is consistent within uncertainty all the way up to around 90×10^3 s (1500 min) thereafter, at long times, as shown in Figure 3.3.
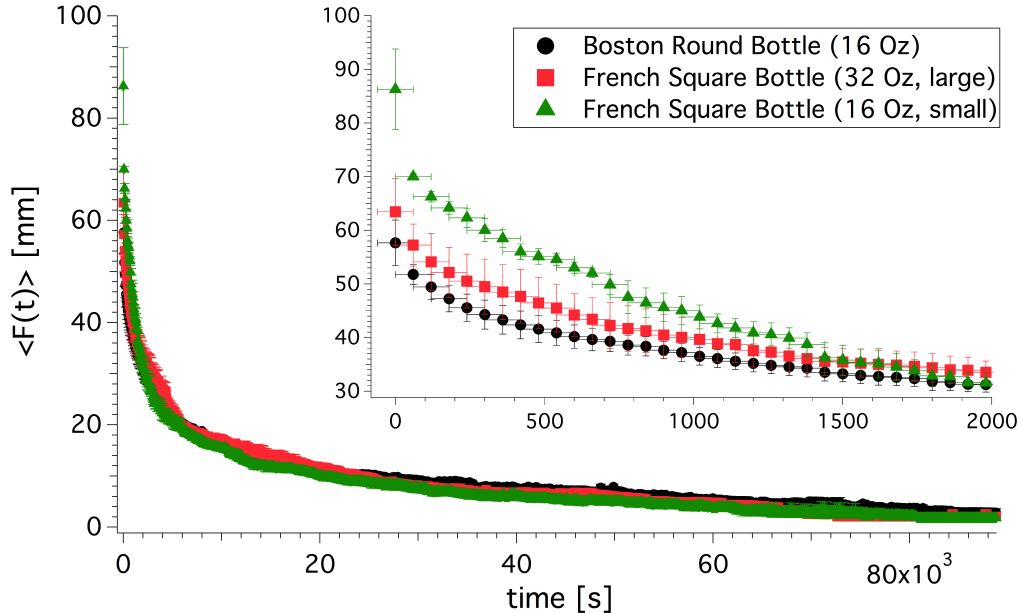

Figure 3.3: Mean foam height, $\langle \mathrm{F(t)} \rangle$, of bulk foams in 3 different glass containers are plotted. The embedded figure shows the first 2000 s (33.3 min). n = 3 trials per container type, 100 mL of a foaming solution per trial was used in each container. Sample: CMC + 0.3wt% (0.0047±0.0002 mol/L) of Triton X-100 surfactant in a 21 g/kg synthetic brine solution.

Aqueous foams are prepared at five different brine concentrations and tested using our dual scale imaging technique. The amount of foaming solutions used is 50 mL (or S = 23 mm). Shown in Figure 3.4 is a converging behavior of the foam and the liquid heights at long times. At the longest times (t $> 55 \times 10^3$ s or 900 min), only the reservoir brine concentration sample shows a different (and higher) foam height. Figure 3.4 (top) shows the error bars of the bulk foam dynamics that correspond to the mean foam height measurement (bottom).

At short times, there are several observations that one can make. First, the initial mean total height, $\langle T(t=0\ s)\rangle$, as a function of brine concentration, shown in Figure 3.5, shows a decreasing trend as the salt concentration (molarity) is increased.
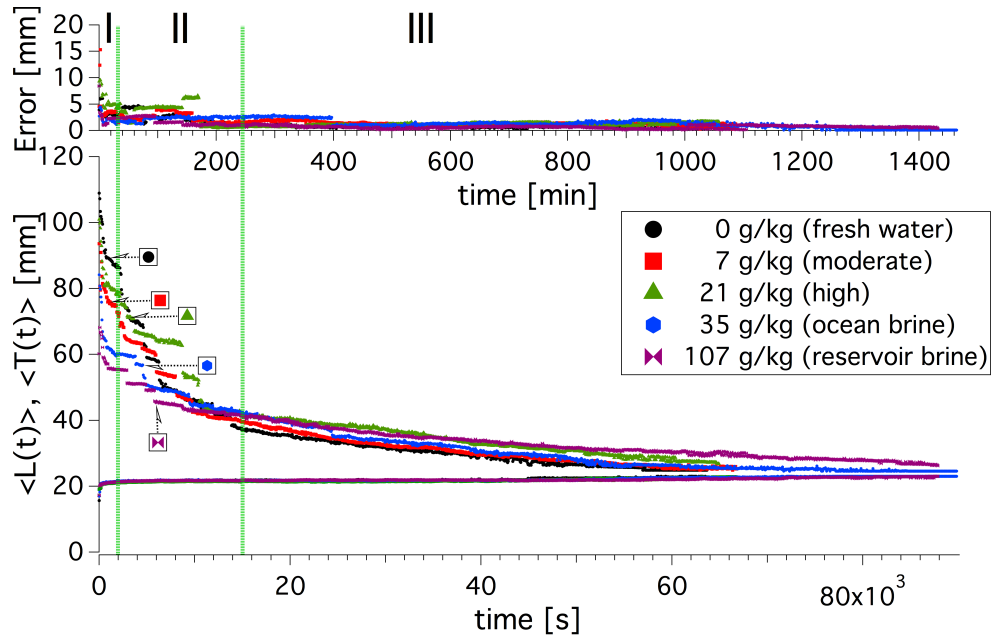

Figure 3.4: Dependence on brine concentration of the mean total and liquid heights. Time regimes I, II and III are separated by the green lines, where region I ranges from 0 s to 2000 s (33.3 min), region II ranges from 2000 s to 15×10^3 s (250 min), and region III ranges from $15 \times 10^3 s$ to the rest. n = 4 trials. The errors represent the standard deviation of the mean total height.
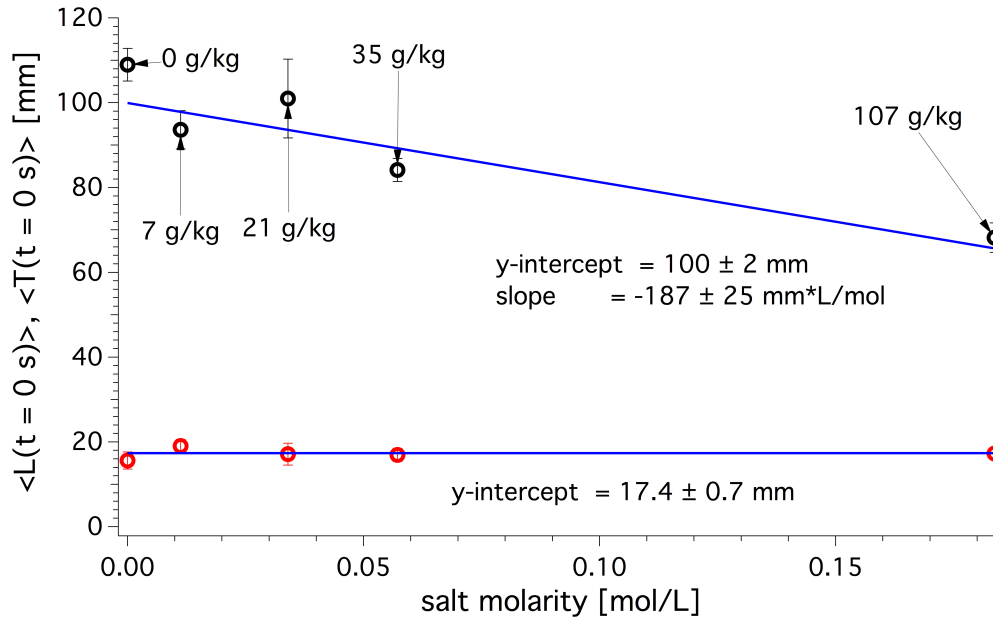
Figure 3.5: Initial mean total height, $\langle T(t=0\ s)\rangle$, and initial mean liquid height, $\langle L(t=0\ s)\rangle$, with varying salinity are compared. The error bars represent the standard deviation of the mean total and liquid heights, respectively. n = 4 trials

In Figure 3.5, the initial total height is plotted for 5 different brine concentrations. The overall trend shows a decrease in the initial total height as the brine concentration increases. The initial liquid height remains relatively the same across all brine concentrations.
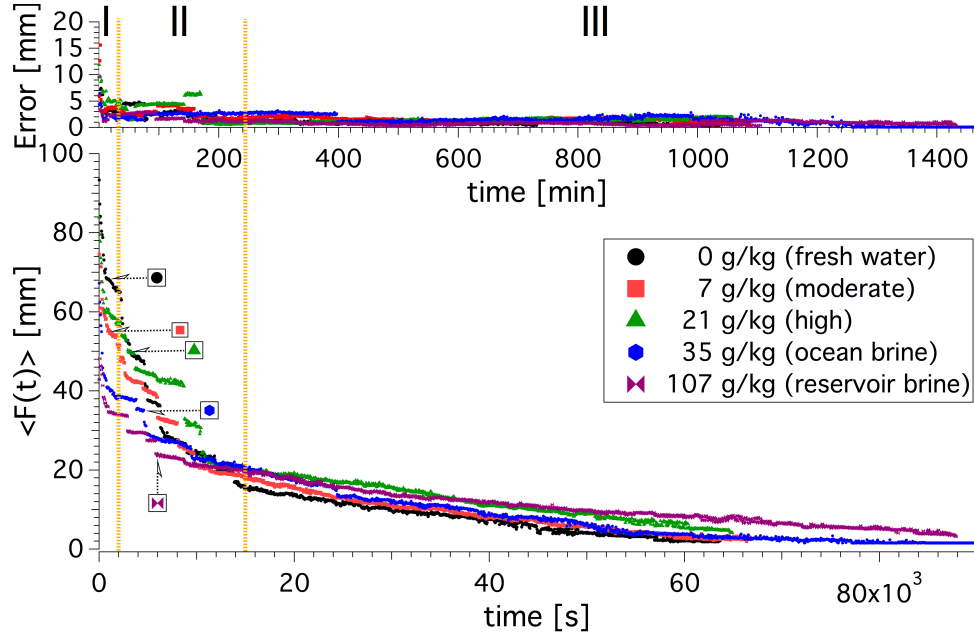
Figure 3.6: Dependence on brine concentration of the mean foam height. Time regimes I, II and III are separated by the yellow lines, where region I ranges from 0 s to 2000 s (33.3 min), region II ranges from 2000 s to 15000 s (250 min, and region III ranges from 15000 s to the rest. n = 4 trials. The error represent the standard deviation of the mean foam height.

Bulk scale dynamics for all brine concentrations, shown in Figure 3.6, are separately analysed in different time regimes. In regime I, rapid foam drainage causes the foam height to decrease for all salinities, as shown in Figure 3.7 (I). In regime II (Figure 3.7 (II)), foam collapse events are frequently observed. Regime II is thus identified as the foam collapse regime. Finally, in regime III ($t > 15 \times 10^3$ s or 250 min), the mean foam height data for all salinities start to converge as shown in Figure 3.7 (III) with the exception of the highest brine concentration, reservoir brine, where foam height is distinctly higher than all other foams beyond 40×10^3 s or 666.7 min.
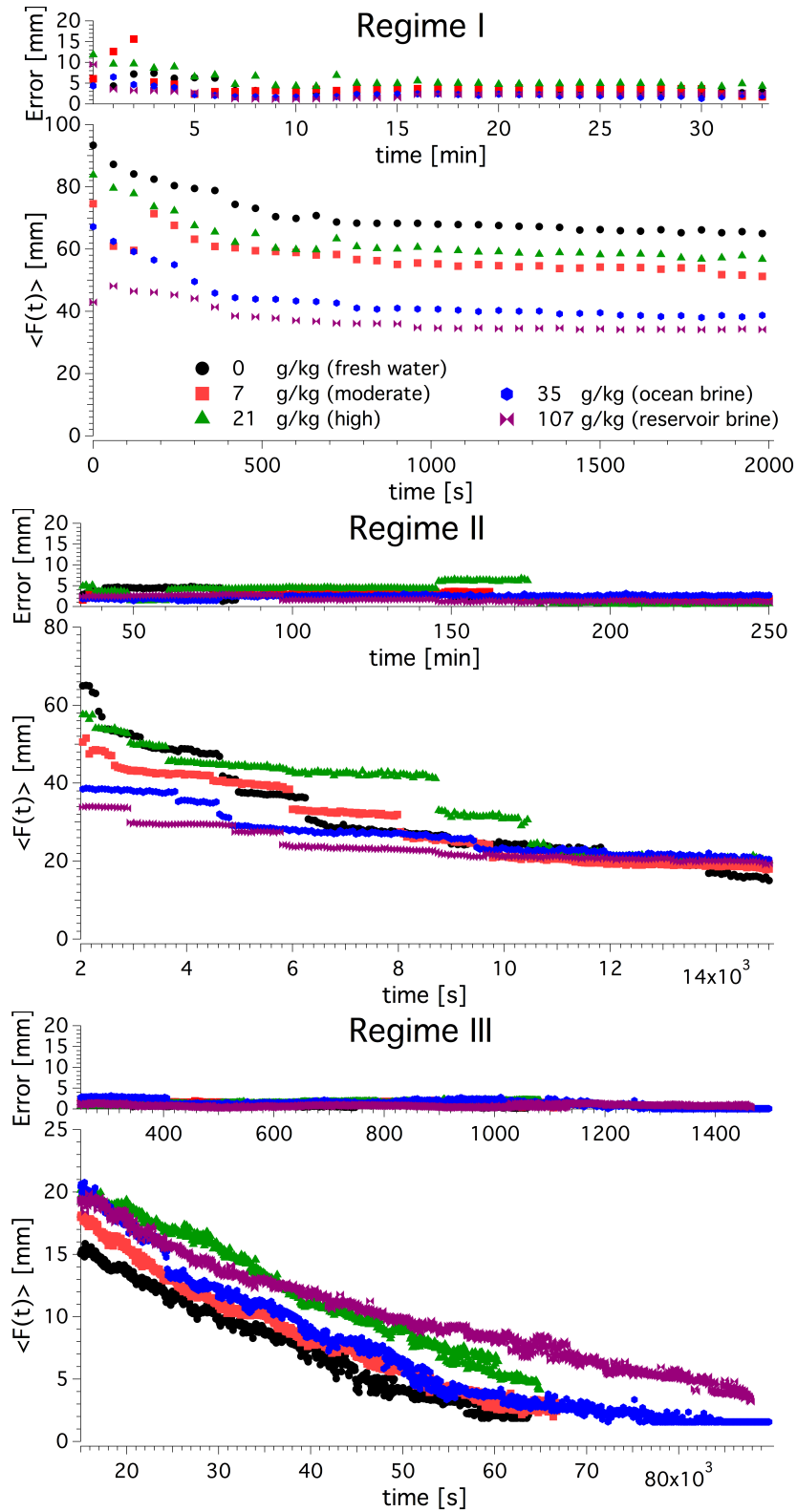
Figure 3.7: Different time regimes of the bulk foam dynamics. Region I ranges from 0 s to 2000 s (33.3 min), region II ranges from 2000 s to 15×10^3 s (250 min), and region III ranges from 15×10^3 s to 90×10^3 s (1500 min).

The short time behavior of the foam is thus apparently not necessarily relevant for long-time stability. We will examine this after we look at the bubble scale dynamics.

3.2   Bubble Scale Foam Dynamics

Having looked at the macroscopic foam height (in the tens of mm) as a function of time, we now look at the bubble scale (sub-mm to mm scale) dynamics.

Figure 3.8 shows some snapshots of bubbles at a height of approximately 24 mm from the bottom of the glass container, approximately 10 mm above the bottom of the foam. From top to bottom, the left-most panel shows one example for a foam (salinity 21 g/kg) at 5 different times (t = 0, 200, 1500, 5000, 9000 s). As can be seen, by about 9×10^3 s (150 min), there are very few bubbles ($\sim$12 detactable bubbles) in the snapshot. Statistics therefore get poorer with time. Also, it is observed, qualitatively, that around the time identified previously as the end of regime I, we see the emergence of faceted droplets (plateau borders). This is also identified in regime II, on the bubble scale, as the start of slow coarsening when all the bubble drainage is completed.

Figure 3.8 (middle panel) shows processed images of bubbles, where the white part represents the bubbles and black part represents the liquid in the foam, from which bubble size distributions (right panel) are obtained. From the bubble size distribution, one can obtain ensemble averages of quantities such as the area.
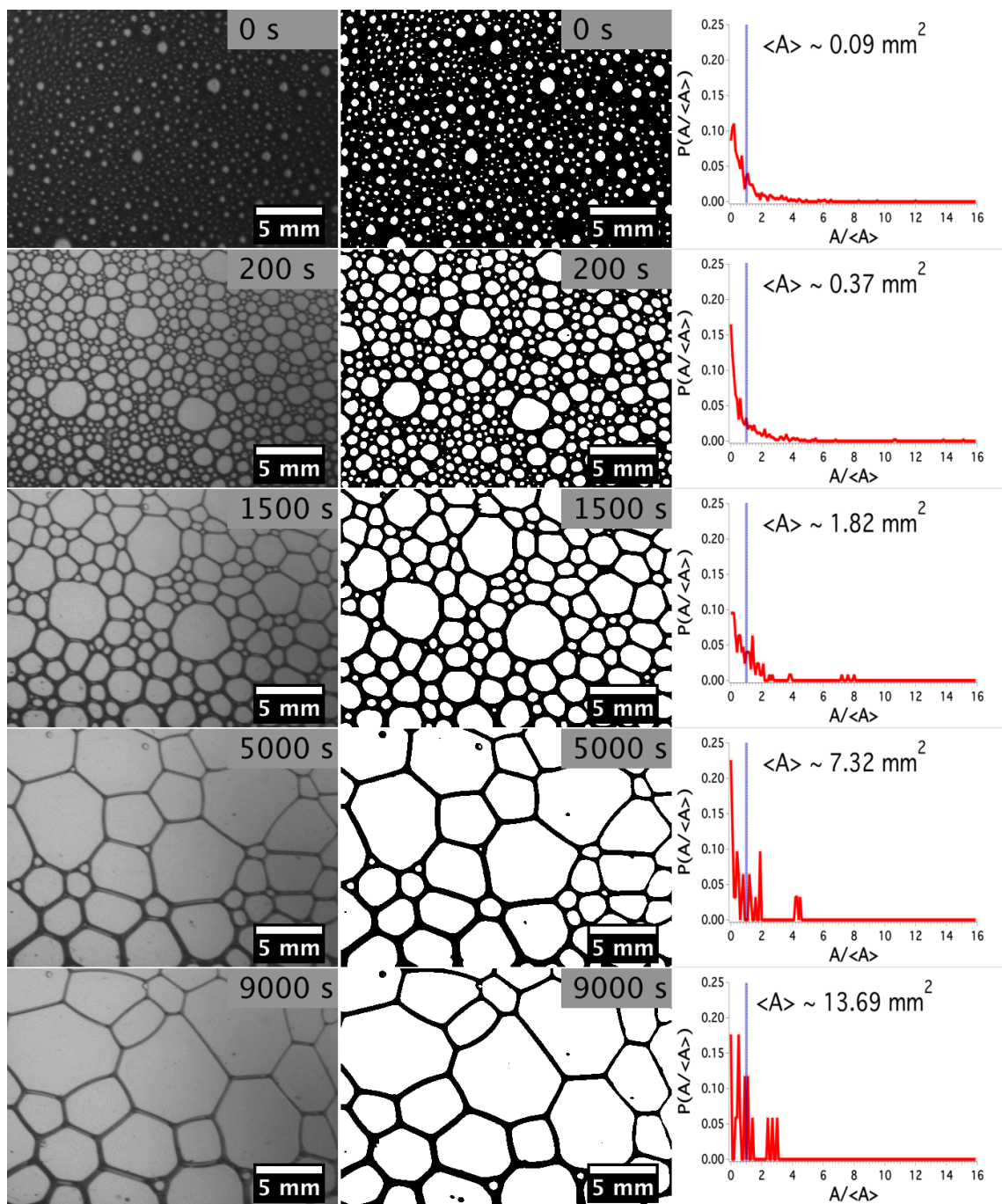
Figure 3.8: Perspective distortion-corrected raw images for different times, their processed images and bubble area distributions are shown. Bubble sizes were obtained from the processed images, excluding the edge bubbles. Blue lines in the area distributions indicate the mean bubble sizes, where A/<A> = 1. Bin size = 160. Bin width = 0.1. Sample: CMC + 0.3wt% (0.0047±0.0002 mol/L) of Triton X-100 surfactant in a 21 g/kg synthetic brine solution (total volume = 100 mL).

time (s)	mean bubble area (mm^2)	root mean square diameter (mm)
0	0.09	0.34
200	0.37	0.69
1500	1.82	1.52
5000	7.32	3.05
9000	13.69	4.18

Table 3.1: A table of mean bubble area and root mean square (rms) diameter for different times shown in Figure 3.8.

Table 3.1 shows the mean buble area and the root mean square diameter (D_{rms}), calculated from the mean bubble area using Equation 3.2 for easy comparison to the scale bars in Figure 3.8.

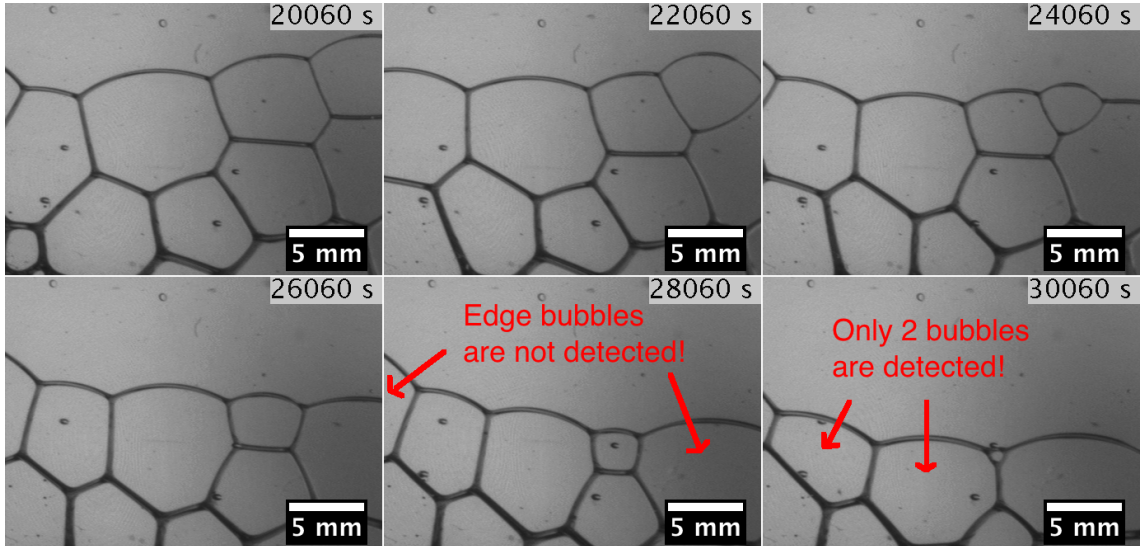$$D_{rms} = \sqrt{\frac{4 \times \langle A \rangle}{\pi}} \tag{3.2}$$

Figure 3.9: Some raw images for different times beyond 20000 s. Number of detectable surface bubbles is small. Sample: CMC + 0.3wt% (0.0047±0.0002 mol/L) of Triton X-100 surfactant in a 21 g/kg synthetic brine solution (total volume = 100 mL).

A sequence of bubble images beyond the 20000 s are shown in Figure 3.9. The incomplete bubbles around the edges of the image are not considered for the bubble
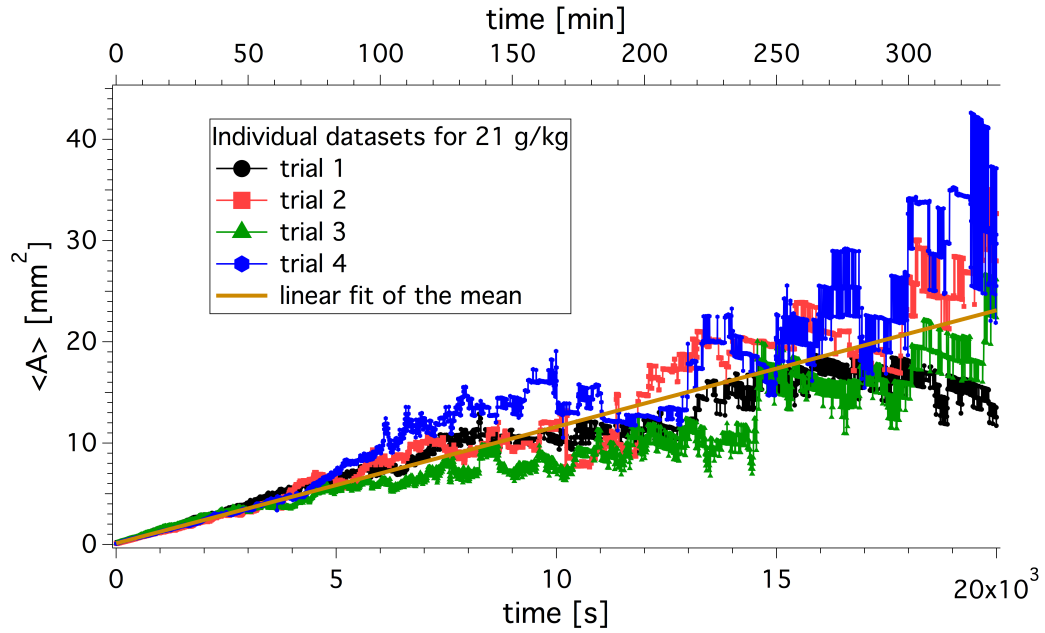
area distribution.

Figure 3.10: The mean bubble area growth of the 21 g/kg foam samples are plotted. The linear fit is the fit of the average of all of the individual 4 trials.

Qualitatively, the mean bubble area (plotted in Figure 3.10) increases with time. Four trials are plotted and exemplify the scatter in the data. In Figure 3.10, the datasets for 4 different trials are fit to a linear function to determine the mean area growth rate. The linear function is defined as follows.

$$\langle A(t) \rangle = K \times t, \tag{3.3}$$

where K is a quantity with units of a diffusion coefficient, but describing a mean bubble area growth rate. This growth rate is consistent with the von-Neumann-Mullins law introduced in Chapter 1. Indeed Equation 1.1 may be rewritten as $\langle A \rangle = Kt$.
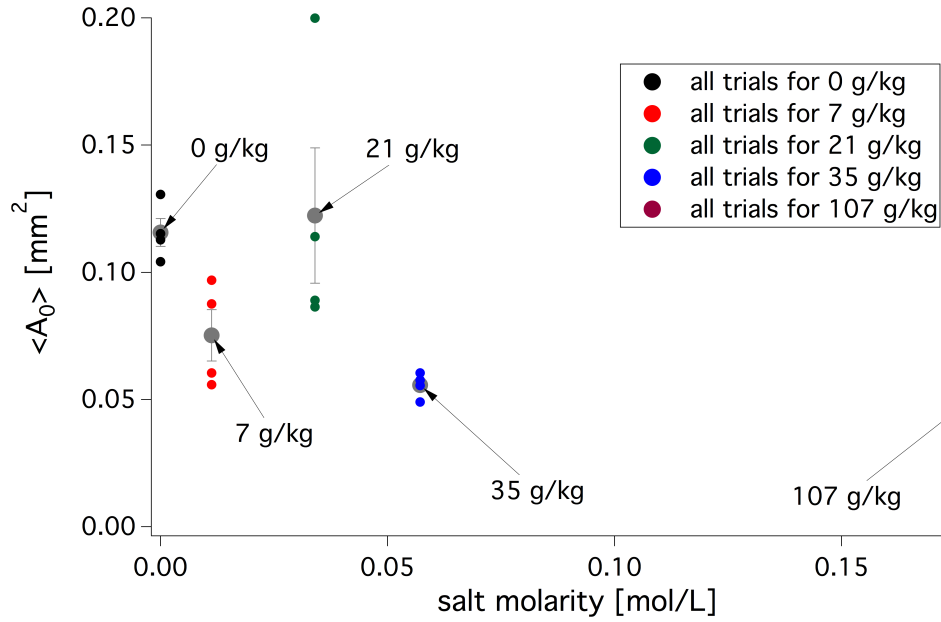
Figure 3.11: Initial mean bubble area for various brine concentration foam samples in the selected region of interest approximately 1 cm above the initial liquid height (S) are shown in grey. The error bars represent the standard deviation of the mean. All trial data for the initial mean bubble area are shown along with the error bars. n = 4 trials.

The initial mean surface bubble area has been plotted for all salinities tested, as shown in Figure 3.11. There is significant scatter in the initial bubble area in multiple runs for the same salinity. This scatter is used to obtain error estimates at each salinity. Within this scatter, there is nevertheless a general decrease in initial bubble area with increasing salinity.
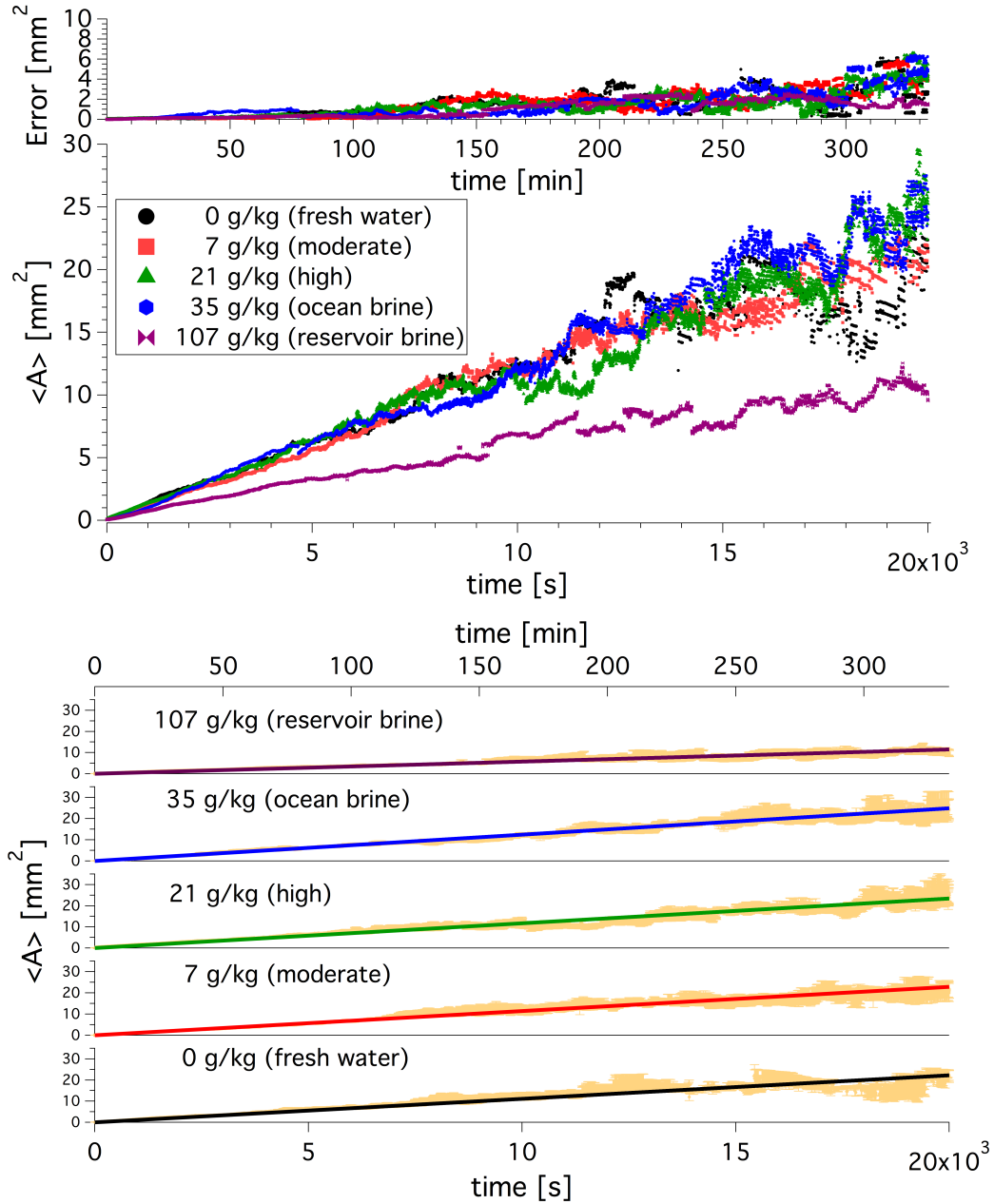
Figure 3.12: Mean bubble area growth for all brine samples are shown. Top: for comparison of the mean area growth for all salinities. Bottom: For comparison of the fits to the mean area growth data for all salinities. A region of interest is selected approximately 1 cm above the initial liquid height, S. n = 4 trials.

All mean bubble area have been plotted with time up to 20,000 s for all salinities, as shown in Figure 3.12. Mean bubble area increases with time for all salinities.

Salt Concentration (g/kg)	K_{mean} (mm^2/s)	standard deviation (mm^2/s)
0	0.0011163	0.0000019
7	0.0011422	0.0000009
21	0.0011721	0.0000012
35	0.0012467	0.0000010
107	0.0005794	0.0000006

Table 3.2: K_{mean} from Figure 3.12 are shown.

This dependence is fit to a linear function (Equation 3.3.) that is based on the von Neumann-Mullins law. This fit is very good, especially at short times, and is reasonable at long times given the noise in the data. The fitted values of the slope, K_{mean}, are tabulated in Table 3.2 for easy comparison.

When all of the datasets are fitted to the linear function, we can extract the K values for all salinities, as plotted in Figure 3.13. This figure shows that increasing salinity level shows consistency from 0 g/kg to 35 g/kg brines, but significantly drops in the growth rate of the mean bubble area for the highest salinity foam. Thus, the highest salinity foam has the lowest mean K.

Based on the combining rules in Figure 1.6, all of the composition of the synthetic brine have been shown to inhibit bubble coalescence. One possibility of the sharp drop in K in Figure 3.13 may be the existence of the transition concentration between the ocean brine (35 g/kg) and the reservoir brine (107 g/kg) concentrations, which may come from the inhibition mechanism of the bubble coalescence. Our foam is the most stable at the reservoir brine concentration.
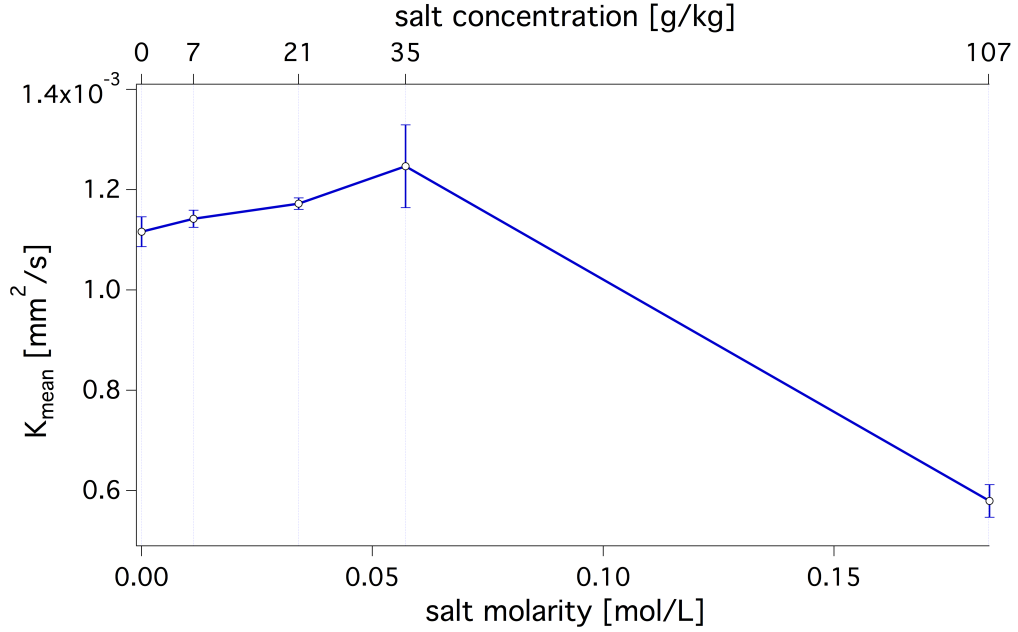
Figure 3.13: The mean bubble area growth rates, K_{mean}, are plotted for all brine concentration foam samples. These values are obtained by fitting the mean area versus time data. The error bars represent the difference of the uncertainties obtained by two different methods. First, the standard error of K values are obtained from fitting all trials area-time data individually. Second, the standard error of K values are obtained from fitting the mean of the area-time data incorporating the standard error from trials area-time data.

3.3   Bulk and Bubble Scale Correlation

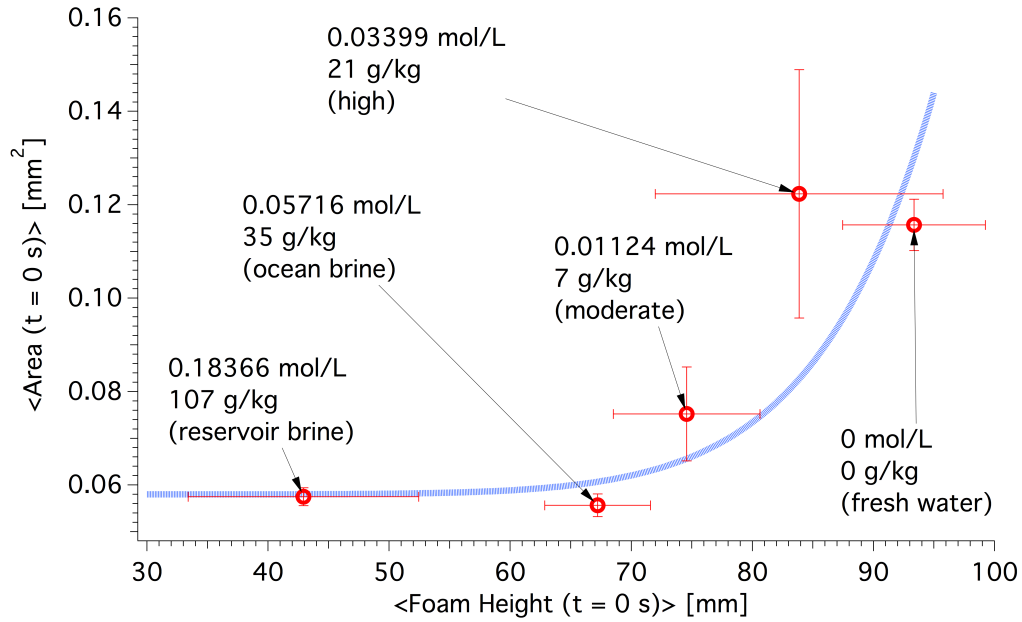Figure 3.14: A correlation between initial mean bubble area and total height ($t = 0$ s) is shown for all salt molarities. The error bars represent the standard deviation of the mean. n = 4 trials. The blue curve is a guide to our eyes.

A broad correlation between the initial mean bubble area (a bubble-scale feature) and the maximum foam height (a bulk-scale feature) is observed: as the initial mean bubble area becomes larger, the mean maximum foam height also becomes larger.

In summary, at bulk scale the lowest salinity had the highest total height initially, but it was also the least stable at long times. So bulk scale imaging revealed that the short time behavior of the foam is not necessarily relevant for long time stability. At the bubble scale, the mean bubble area of salinity foams from 0 g/kg to 21 g/kg salinity levels show some consistencies in mean area, above which drops significantly. From 0 s to 20,000 s, the mean bubble area of all salinities linearly increase with time, as shown in Figure 3.12. This is consistent with von Neumann-Mullins scaling [1]. Due to the poor statistics in bubble number beyond 20,000 s, it is not clear if this scaling holds at longer times.

From the slopes of these plots, one can obtain the growth rate of the mean bubble area. This growth rate K is seen not to depend much on salinity with the exception of the highest salinity, reservoir brine. It is remarkable that while this information is only apparent at very long times with bulk scale imaging, it is already apparent at early times in bubble scale imaging close to the liquid meniscus.

Chapter 4

Conclusions

For our foam stability study, we investigated an entire decay of evolution of $3D$ aqueous foams in the presence of synthetic ocean brine at five different concentrations. We first developed an imaging system that could measure bulk-scale foam stability and bubble coarsening dynamics simultaneously, in an automated way, to individually probe these mechanisms at different length scales over the foam's lifetime. We then examined three different shaped and sized bottles (16 Oz French Glass Bottle, 32 Oz French Glass Bottle and 16 Oz Boston Round Bottle) to identify the optimal bottle for further study by looking their initial foam height. We chose the 16 Oz French Glass Bottle due to resulting in the highest initial foam height, and it was within the allowed bottle height of 13.0 cm. This condition needed to be met to prevent from sudden foam collapses from bubble detachment at the top part of the enclosed bottle and to minimize the effect of bottles on the foam stability. At the bulk scale, we followed the evolution of foam height for approximately 90,000 seconds ($\sim$25 hours). We observed three regimes of behavior. In Regime I, between 0 and 2,000 seconds (or 33.3 minutes), rapid foam drainage caused the foam height to decrease for all salinities. In Regime II, between 2,000 and 15,000 seconds (250 minutes), foam collapse events were frequently

observed. In Regime III, from 15,000 seconds and on, all foams converged in foam height, with one exception: the highest salinity brine (reservoir brine) foam had a much smaller decrease in foam height, as shown in Figure 3.7.

At the bubble scale, we probed and analyzed the foam for 20,000 seconds (333.3 minutes): beyond this time the number of bubbles became statistically inadequate. In all cases, a region of interest 1 cm above the meniscus was chosen for the bubble-scale measurement. In Regime I as defined in the case for the bulk scale dynamics, the mean area of the bubbles (in the region of interest) showed steady increase with time for all salinities. The mean bubble area grew linearly with time, and the growth rates were consistent for all salinities, but once again with the lone exception of the highest salinity. In Regime II, mean bubble area of the highest salinity bubbles and the rest of the bubbles continued to diverge. In Regime III, all salinity bubbles showed high fluctuations in mean area, as shown in Figure 3.12. Overall, the highest salinity bubbles coarsened the slowest.

Comparing the bulk and bubble scale information, as the salt concentration was increased, the foam height decreased and so did the mean bubble area, i.e., bulk and bubble scale information was correlated, as shown in Figure 3.14. At the bulk scale, approximately 15000 seconds of data was required to show that the highest brine concentration foam was the most stable. For the bubble scale, however, only 3600 seconds of data was required to show this effect of high salinity on foam. This, we believe, is a notable result.

On understanding of the ion-specific bubble coalescence inhibition mechanism, a number of studies [22–26] have proposed possible mechanisms, yet interpretation and explanation of empirically shown results require further theoretical investigation [27]. Our experimental results are in good agreement with the ion-specific observations at the highest salt concentration as the synthetic ocean brine contains salts that are

empirically shown to inhibit bubble coalescence, as shown in Figure 1.6. Thus, the ion-specific effect likely has played a major role in the overall foam stability with the highest salinity foam to be the most stable foam, as shown in both our bulk scale (Figure 3.6) and bubble scale (Figure 3.12) data.

While further investigation is necessary to understand the concentration dependence of salinity on foams, we postulate that the possible physical mechanism behind the overall foam stability at the reservoir brine is due to bubble coalescence inhibition mechanism (or "film rupturing") by specific types of salt in synthetic ocean brine. As discussed in the Introduction, bubble coalescence is one of the foam stability mechanisms. As shown in the bulk-scale imaging experiments, this coalescence effect is apparent at long times; foams show the highest overall stability at highest salinity. A parameter determined from bubble scale imaging, the mean bubble growth rate in the foam, K, is a determinant of foam stability. K is roughly constant (slightly increasing) up to 35 g/kg, but appears to decrease sharply between 35 g/kg and 107 g/kg. This behavior needs to be examined further.

At short times, on average, the lowest salinity foam had the highest initial foam height, while the highest salinity foam had the lowest initial foam height. In contrast, clear trend was not observed at the bubble scale. At intermediate times, as foam drainage and collapse happened, the mean bubble area for all salinities steadily increased at different rates at near the liquid meniscus. At long times, the highest salinity foam was observed to remain strong, while all other salinities lost bubbles due to the pressure gradient with the ambient pressure in the glass bottle.

While physical parameters, such as the bubble size and the foam height do not define the entire characteristics of a foam, by integrating the information obtained from the bulk and bubble scales, one can estimate different regimes in foam stability mechanisms, by which we may be able to identify the onsets and offsets of different

mechanisms that are typically hidden if we only focused on information from one length scale measurement.

We have gained some understanding of the ocean brine contribution to the stability of a non-ionic foam using our simultaneous imaging technique. This study is of relevance to the oil industry on a potential candidate fluid choice for oil extraction from oil reservoirs, and the testing method will likely contribute to standardizing a bulk- and bubble-scale characterization method for future foam stability studies.

Chapter 5

Future Work

We have gained insights into the physics questions posed in Introduction in the context of foam stability at different salt concentrations. For future work, one of the interesting aspects to look into, is further quantitative investigation on the different time regimes of foam dynamics that are qualitatively identified in Figure 3.7, and discussed the results based on our experimental approach for a deeper understanding of the salt concentration dependence of foam stability.

In Regime I, where we identified as the dynamic regime of a rapid liquid drainage through the plateau border in foam, a sharp increase in liquid height is observed at the shortest times for all salinities. During this time regime, the sharp increase in liquid height at the bulk scale indicates that the liquid is rapidly flowing through the foam in the direction of gravity, where we force drain the liquid. This liquid drainage may or may not affect the concurrent dynamics with the bubble growth. In Regime II, where we identified as the dynamic regime of frequent foam collapses, the foams are observed to be destabilized at all length scales. Further analysis on the intensity fluctuation of the bulk-scale foam through the crossed polarizer may provide an indication or signature of these catastrophic events prior to happening

at timescales shorter than sub-seconds. What is the origin of these catastrophies? In Regime III, where we identified as the dynamic regime of the convergence in all salinity foams at the bulk-scale, except the foam with the highest salinity. A further investigation on the stability of foam at the liquid film scale may provide insights into stability mechanism of the foams at all salinities.

While our work focuses on the foam dynamics at the bulk scale in foam height and the bubble scale at a bottle surface, there are complimentary techniques that would help to correlate our results. $3D$ nuclear magnetic resonance imaging, for instance, allows us to measure the liquid content in a foam and structural data can also be obtained. The dynamics of foam in $3D$ can be studied. Visco-elasticity of foams can also be probed using rheological methods.

Along with further investigation on theoretical understanding of specific salt contributions to foam stability, investigations at all length and time scales in foam with high temporal and spatial resolutions and using the complementary techniques mentioned above would open up new opportunities for future foam research.

Thorough characterization of potential foams at the fundamental level will provide further insights into important factors in deciding potential candidate fluids for enhanced oil recovery applications. In this work, we show the importance of investigating reservoir brine effects on foams at all length and time scales for future foam studies.

Bibliography

[1] Eugene M. Terentjev and David A. Weitz. *The Oxford Handbook of Soft Condensed Matter*. Oxford University Press, 2015.

[2] University of Cambridge The Cavendish Laboratory, Department of Physics. Length scales in complex fluids, 2017.

[3] Dominique Langevin. Aqueous foams and foam films stabilised by surfactants. Gravity-free studies. *Comptes Rendus Mécanique*, 345(1):47–55, 2017.

[4] Wiebke Drenckhan and Stefan Hutzler. Structure and energy of liquid foams. *Advances in Colloid and Interface Science*, 224:1–16, 2015.

[5] Ismael Fortuna, Gilberto L. Thomas, Rita M. C. de Almeida, and François Graner. Growth Laws and Self-Similar Growth Regimes of Coarsening Two-Dimensional Foams: Transition from Dry to Wet Limits. *Physical Review Letters*, 108(24):248301, 2012.

[6] François G. Gandolfo and Henri L. Rosano. Interbubble Gas Diffusion and the Stability of Foams. *Journal of Colloid and Interface Science*, 194(1):31–36, 1997.

[7] Arnaud Saint-Jalmes. Physical chemistry in foam drainage and coarsening. *Soft Matter*, 2(10):836–849, 2006.

[8] Robert D. MacPherson and David J. Srolovitz. The von Neumann relation generalized to coarsening of three-dimensional microstructures. *Nature*, 446:1053, 2007.

[9] Douglas J. Durian, David A. Weitz, and David J. Pine. Dynamics and coarsening in three-dimensional foams. *Journal of Physics: Condensed Matter*, 2(S):SA433, 1990.

[10] Jianlong Wang, Say Hwa Tan, Anh V. Nguyen, Geoffrey M. Evans, and Nam-Trung Nguyen. A Microfluidic Method for Investigating Ion-Specific Bubble Coalescence in Salt Solutions. *Langmuir*, 32(44):11520–11524, 2016.

[11] Standard test method for foam in aqueous media (bottle test), 2007.

[12] Wiebke Drenckhan and Arnaud Saint-Jalmes. The science of foaming. *Advances in Colloid and Interface Science*, 222:228–259, 2015.

[13] Mahsa Moayedi. An experimental study on surfactant-alternating-gas process. Master's thesis, Memorial University of Newfoundland, 2015.

[14] Alexey Andrianov, Rouhi Farajzadeh, M. Mahmoodi Nick, M. Talanana, and Pacelli L. J. Zitha. Immiscible Foam for Enhancing Oil Recovery: Bulk and Porous Media Experiments. *Industrial & Engineering Chemistry Research*, 51(5):2214–2226, 2012.

[15] Bernard P. Binks and Tommy S. Horozov. Aqueous Foams Stabilized Solely by Silica Nanoparticles. *Angewandte Chemie International Edition*, 44(24):3722–3725, 2005.

[16] Kofi Osei-Bonsu, Nima Shokri, and Paul Grassia. Foam stability in the presence and absence of hydrocarbons: From bubble- to bulk-scale. *Colloids and Surfaces A: Physicochemical and Engineering Aspects*, 481:514–526, 2015.

[17] D. J. Durian, D. A. Weitz, and D. J. Pine. Scaling behavior in shaving cream. *Physical Review A*, 44(12):R7902–R7905, 1991.

[18] Maria Papara, Xenophon Zabulis, and Thodoris D. Karapantsios. Container effects on the free drainage of wet foams. *Chemical Engineering Science*, 64(7):1404–1415, 2009.

[19] Barry W. Ninham and Pierandrea Lo Nostro. *Molecular Forces and Self Assembly in Colloids, Nanosciences and Biology.* Cambridge University Press, 2010.

[20] Christine L. Henry, Casuarina N. Dalton, Lehoa Scruton, and Vincent S. J. Craig. Ion-Specific Coalescence of Bubbles in Mixed Electrolyte Solutions. *The Journal of Physical Chemistry C*, 111(2):1015–1023, 2007.

[21] Vincent Craig, Barry Ninham, and Richard Mark Pashley. Effect of electrolytes on bubble coalescence. *Nature*, 364(6435):317–319, 1993.

[22] S. J. Miklavcic. Deformation of fluid interfaces under double-layer forces stabilizes bubble dispersions. *Physical Review E*, 54(6):6551–6556, 1996.

[23] Benjamin S. Chan and Ying Hang Tsang. A theory on bubble-size dependence of the critical electrolyte concentration for inhibition of coalescence. *Journal of Colloid and Interface Science*, 286(1):410–413, 2005.

[24] H. K. Christenson, R. E. Bowen, J. A. Carlton, J. R. M. Denne, and Y. Lu. Electrolytes that Show a Transition to Bubble Coalescence Inhibition at High Concentrations. *The Journal of Physical Chemistry C*, 112(3):794–796, 2008.

[25] Vassili V. Yaminsky, Satomi Ohnishi, Erwin A. Vogler, and Roger G. Horn. Stability of Aqueous Films between Bubbles. Part 1. The Effect of Speed on Bubble Coalescence in Purified Water and Simple Electrolyte Solutions. *Langmuir*, 26(11):8061–8074, 2010.

[26] Phong T. Nguyen and Anh V. Nguyen. Drainage, Rupture, and Lifetime of Deionized Water Films: Effect of Dissolved Gases? *Langmuir*, 26(5):3356–3363, 2010.

[27] Mahshid Firouzi and Anh V. Nguyen. The Gibbs-Marangoni stress and nonDLVO forces are equally important for modeling bubble coalescence in salt solutions. *Colloids and Surfaces A: Physicochemical and Engineering Aspects*, 515:62–68, 2017.

[28] Jenny Higgins. Oil Industry and the Economy, 2017.

[29] G M Homsy. Viscous Fingering in Porous Media. *Annual Review of Fluid Mechanics*, 19(1):271–311, 1987.

[30] Wei Yan, Clarence A. Miller, and George J. Hirasaki. Foam sweep in fractures for enhanced oil recovery. *Colloids and Surfaces A: Physicochemical and Engineering Aspects*, 282-283:348–359, 2006.

[31] Phong Nguyen, Hossein Fadaei, and David Sinton. Nanoparticle Stabilized CO2 in Water Foam for Mobility Control in Enhanced Oil Recovery via Microfluidic Method. 2014.

[32] Fisher BioReagents. Triton x-100 (electrophoresis). Technical report, Fisher Scientific.

[33] Sigma-Aldrich. Suggestions for cleaning glassware. Technical report.

[34] DOW. Triton x-100 surfactant technical specifications. Technical report, The Dow Chemical Company, 2017.

[35] Union Carbide. Triton x-100 surfactant material safety data sheets. Technical report, Union Carbide Corporation, 2000.

[36] Fisher Scientific. Triton x-100 surfactant safety data sheet. Technical report, Thermo Fisher Scientific, 2014.

[37] Daoyong Yu, Fang Huang, and Hai Xu. Determination of critical concentrations by synchronous fluorescence spectrometry. *Analytical Methods*, 4(1):47–49, 2012.

[38] Mukesh Lavkush Bhaisare, Sunil Pandey, M. Shahnawaz Khan, Abou Talib, and Hui-Fen Wu. Fluorophotometric determination of critical micelle concentration (CMC) of ionic and non-ionic surfactants with carbon dots via Stokes shift. *Talanta*, 132:572–578, 2015.

[39] Uttam Anand, Chandrima Jash, and Saptarshi Mukherjee. Spectroscopic determination of Critical Micelle Concentration in aqueous and non-aqueous media using a non-invasive method. *Journal of Colloid and Interface Science*, 364(2):400–406, 2011.

[40] Sigma Aldrich. Triton x-100 product information. Technical report, 1999.

[41] Abdulrazaq Zubair. *Design and Optimization of Surfactant Based Enhanced Remediation of Bunker C Fuel Oil Contaminated Soil.* PhD thesis, Memorial University of Newfoundland, 2015.

[42] Mei Li, Yahya Rharbi, Xiaoyu Huang, and Mitchell A. Winnik. Small Variations in the Composition and Properties of Triton X-100. *Journal of Colloid and Interface Science*, 230(1):135–139, 2000.

[43] U.S. Geological Survey's Water Science School. Saline water (https://water.usgs.gov/edu/saline.html).

[44] DMA 35 Portable Density Meter Instruction Manual. Technical report, Anton Paar, 2010.

Appendix A

Appendix: Density, viscosity, conductivity and surface tension

A.1 frequency-specific density of the foaming solution

A hand-held densitometer was used to measure the density of the deionized water and solutions at 5 different brine concentrations at a constant temperature ($T = 21.2° \pm 0.1°$). We find that density of the foaming solution increases linearly as the salt molarity is increased, as shown in Figure A.1.
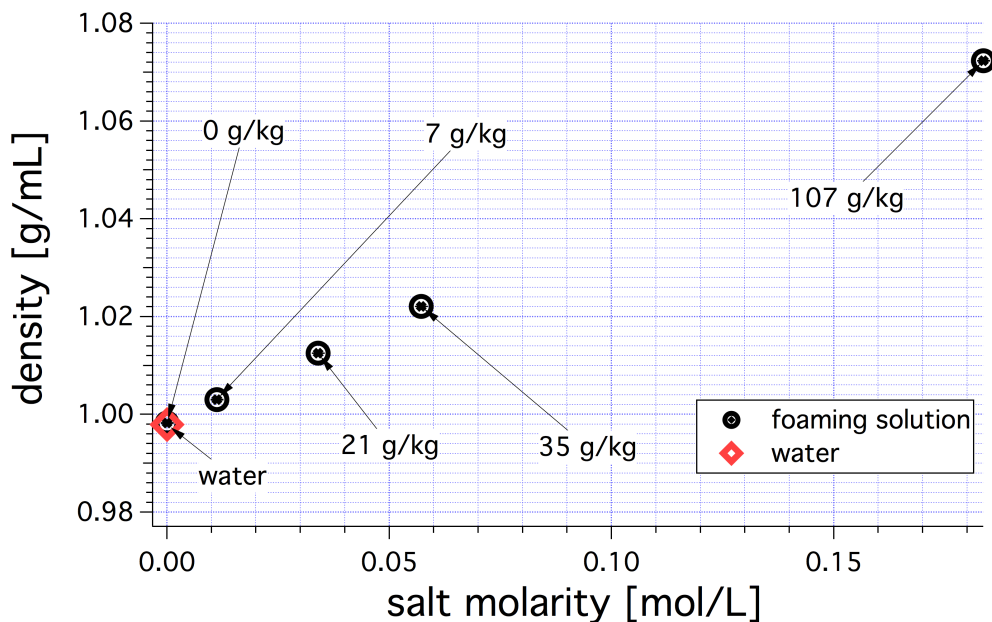
Figure A.1: Density of the solutions is plotted against salt molarity of the samples. The red marker represents the density of water, which was measured in between each sample measurement and resulted in a consistent value of 0.9979 g/mL every time at a constant temperature $T = 21.2° \pm 0.1°$. We ensured no frequency-specific density change due to contamination or existence of bubbles in solutions. The error bars exist within the data point markers. n = 3 trials. Sample: 0.0047 ± 0.0002 mol/L of TX100 surfactant in various brine concentrations.

A.2   interfacial property of the foaming solutions

An interfacial tension meter was used to measure the surface tension of the deionized water and solutions at 5 different brine concentrations at a constant room temperature $T = 21.5° \pm 0.5°$. We find that on average, surface tension of the deionized water decreases from 71.369 mN/m to 30.575 mN/m when 0.0047 ± 0.0002 mol/L or 2.82 mL of TX-100 surfactant in 1 kg of solution is added, as shown in Figure A.2. We also find that surface tension of the solutions stay at a relatively constant surface tension value, on average at 31.6 ± 0.4 mN/m, for all brine samples at various concentrations.
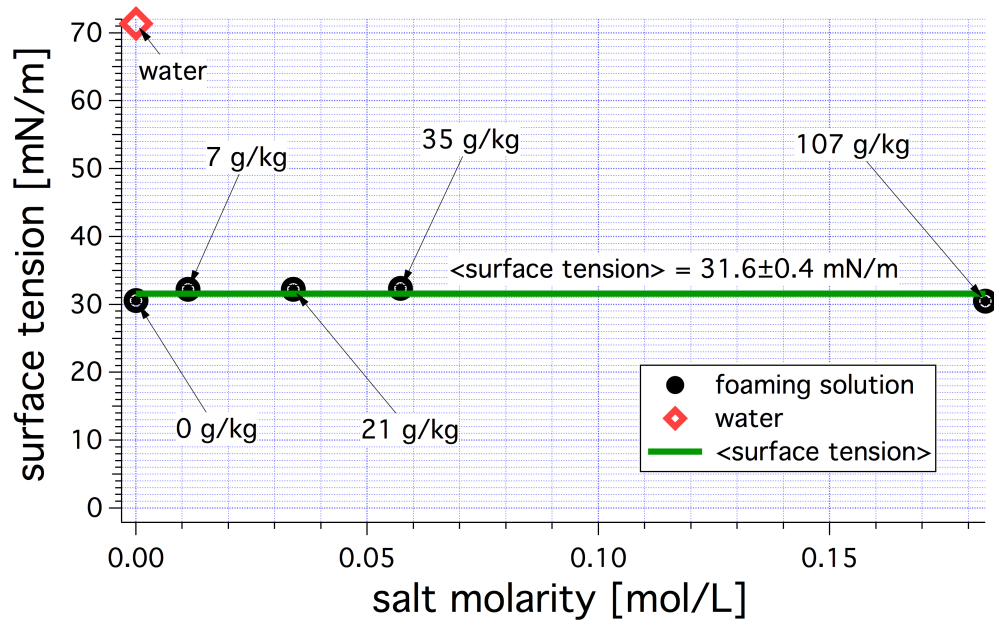
Figure A.2: Surface tension of the solutions is plotted against salt molarity of the samples. The red marker represents the surface tension of water. The error bars exist within the data point markers. n > 10 trials for all foaming solutions. Sample: 0.0047 ± 0.0002 mol/L of TX100 surfactant in various brine concentrations.

In the range of 30 mN/m to 34 mN/m, we find that brine concentrations at 7 g/kg, 21 g/kg and 35 g/kg samples are significantly different from 0 g/kg and 107 g/kg surface tension values, as shown in Figure A.3.
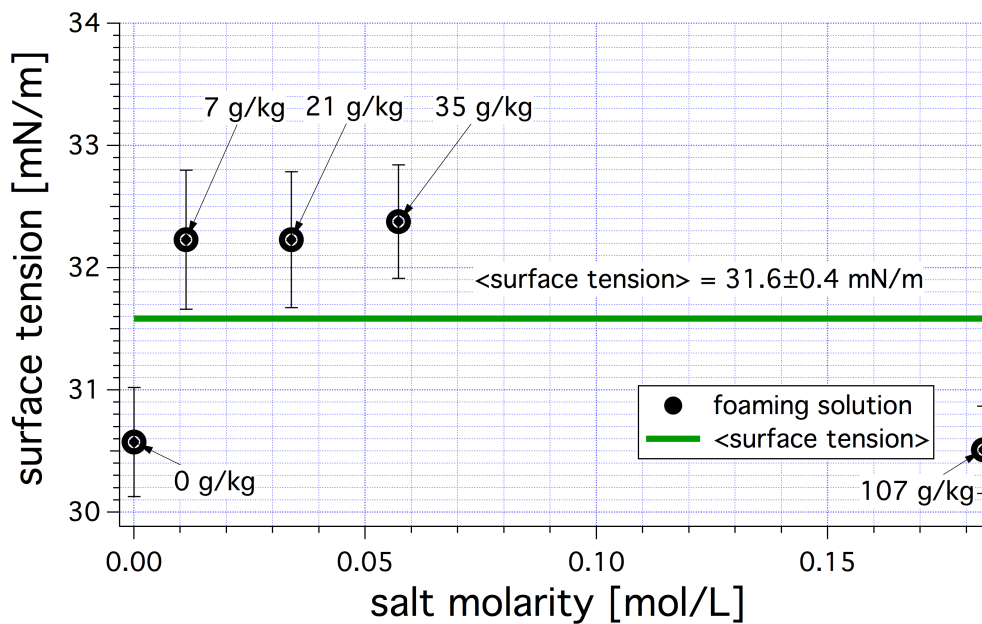
Figure A.3: Surface tension of the solutions is plotted against salt molarity of the samples. This is the selected range of Figure A.2. The error bars exist within the data point markers. n > 10 trials for all foaming solutions. Sample: 0.0047 ± 0.0002 mol/L of TX100 surfactant in various brine concentrations.

A.3   rheological property of the foaming solutions

A rheometer was used to measure the viscosity of the deionized water and solutions at 5 different brine concentrations at a constant room temperature. We find that overall, the viscosity of the solutions increases as their salt molarity is increased with the exception of the 35 g/kg sample, as shown in Figure A.4.
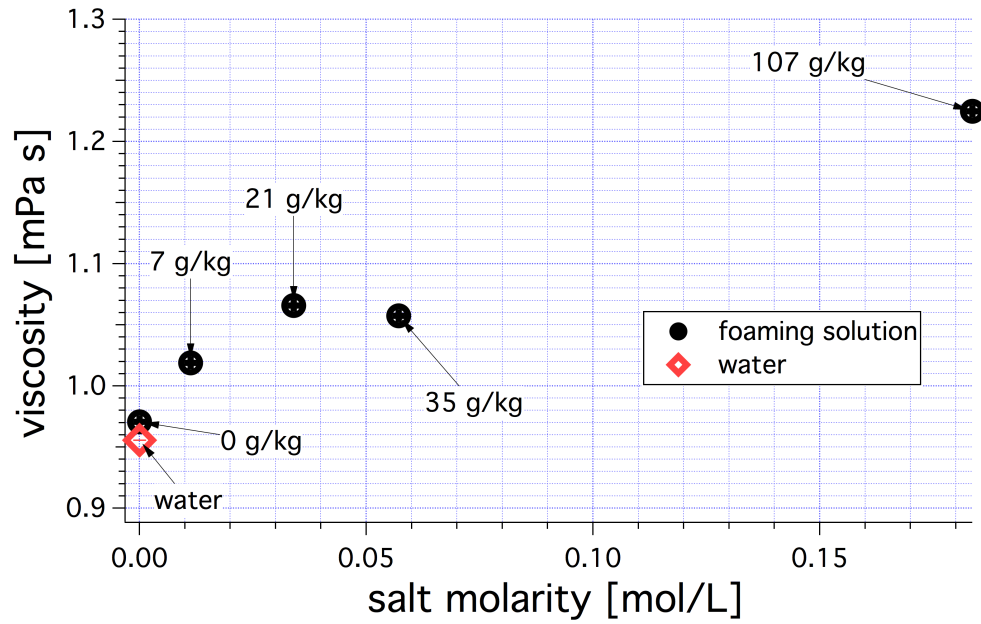
Figure A.4: Viscosity of the solutions and deionized water are plotted against salt molarity of the samples. The red marker represents the viscosity of water. Sample: 0.0047 ± 0.0002 mol/L of TX-100 surfactant in various brine concentrations.